Monthly Notices of the ROYAL ASTRONOMICAL SOCIETY

MNRAS **548,** 1–19 (2026) https://doi.org/10.1093/mnras/stag745
Advance Access publication 2026 April 20

Binary and neutron star evolution in low-mass X-ray binaries on the evolutionary tracks of accreting millisecond X-ray pulsars

N. Niang [1]★ Ü. Ertan [1] A. A. Gençali [1] F. Ertuğrul [1] A. Ulubay,[2]
E. Devlen [3] and M. A. Alpar [1]

[1]*Faculty of Engineering and Natural Sciences, Sabancı University, Orhanlı, Tuzla 34956, İstanbul, Turkey*
[2]*Faculty of Science, Department of Physics, Istanbul University, Vezneciler 34134, İstanbul, Turkey*
[3]*Faculty of Science, Department of Astronomy and Space Sciences, Ege University, Bornova 35100, İzmir, Turkey*

Accepted 2026 April 17. Received 2026 March 29; in original form 2025 November 18

ABSTRACT

Neutron star low-mass X-ray binaries (LMXBs) are the progenitors of millisecond pulsars. In these systems, old neutron stars (NSs) can be spun up during a long-lasting accretion phase. The discovery of accreting millisecond X-ray pulsars (AMXPs) and transitional millisecond pulsars has provided key observational insights into the connection between millisecond pulsars and LMXBs. In this work, we have investigated both the binary system and the individual NS evolution leading to AMXP properties. We use `mesa` to analyse the binary evolution of LMXBs, following three distinct evolutionary tracks defined by the AMXP donor types. We find that while the magnetic braking index may affect the mass-transfer history, the initial orbital period is the most influential parameter that shapes the overall binary evolution. We use the mass accretion histories estimated from these binary simulations to study the rotational evolution of NSs employing the model that can account for torque–luminosity relations and the lack of X-ray pulses from most of these systems. With reasonable model parameters, our model results are in agreement with the typical properties of AMXPs. For these AMXP sources from each evolutionary track, we have shown that the model can reproduce the NS and binary properties simultaneously. Finally, we discuss the time-scales of different evolutionary paths, as well as the conditions under which these systems could be detectable at various stages of their evolution.

Key words: accretion, accretion discs – stars: neutron.

1 INTRODUCTION

In neutron star (NS) low-mass X-ray binaries (LMXBs), the compact object accretes matter from its low-mass companion with mass $M_2 < 1\,M_\odot$ through Roche lobe overflow (RLOF) in a close binary (with orbital period $P_{\rm orb} < 1$ d). NSs in LMXBs can be spun up to millisecond periods through accretion torques (M. A. Alpar et al. 1982; V. Radhakrishnan & G. Srinivasan 1982). This process, so-called *recycling scenario*, positions the LMXBs as the progenitors of weakly magnetized radio millisecond pulsars (RMSPs) (for a review see G. Srinivasan 2010). First observational support for this scenario came with the discovery of coherent 2.5 ms X-ray pulsations from the first accreting millisecond X-ray pulsar (AMXP) SAX 1808.4-3656 (R. Wijnands & M. Van Der Klis 1998). At present, there are 23 known AMXPs (A. Patruno & A. L. Watts 2021). The recently discovered three transitional millisecond pulsars (tMSPs), which show transitions between the X-ray pulsar and radio pulsar states, have provided the missing link connecting LMXBs to RMSPs (A. M. Archibald et al. 2009; A. Papitto et al. 2013; C. G. Bassa et al. 2014; A. Papitto & D. de Martino 2022).

The long-term evolution of LMXBs can be summarized as follows: (i) In the first stage, the source is spun up by the mass accretion on to the NS (at rates close to the Eddington limit). The accretion also causes the rapid decay of the magnetic field through ohmic dissipation (G. Srinivasan et al. 1990; U. Geppert & V. Urpin 1994; V. Urpin & U. Geppert 1995; S. Konar & D. Bhattacharya 1997). The dipole field is expected to freeze at a strength of a few 10^7–10^9 G in correlation with the accretion rate in the early stages of the evolution (S. Konar & D. Bhattacharya 1997; G. Srinivasan 2010). (ii) In the subsequent phase, the mass inflow rate of the disc, $\dot{M}_{\rm in}$, decreases and the system is likely to be observed as a transient source like AMXPs. With further decrease in $\dot{M}_{\rm in}$, the binary goes through a Roche lobe (RL) decoupling phase (T. M. Tauris 2012). (iii) In the final LMXB phase with the lowest $\dot{M}_{\rm in}$ levels, the system could become a tMSP, and eventually becomes an RMSP after the NS enters the strong propeller (SP) phase.

The observed properties of AMXPs summarized in Table 1 categorize them into three distinct groups: The first group consists of nine sources with main sequence (MS) companions of mass $0.1\,{\rm M}_\odot < M_2 < 0.5\,{\rm M}_\odot$ and $3\,{\rm h} < P_{\rm orb} < 19$ h. These sources are the fastest spinning AMXPs with median spin period $\langle P \rangle \simeq 2.2$ ms. The second group includes four sources with low-mass ($M_2 \simeq 0.01\,{\rm M}_\odot$) degenerate brown dwarf (BD) companion and 1 h <

★ E-mail: niang@sabanciuniv.edu

Table 1. Observed properties of 23 AMXPs. The distance, d, and $L_{\rm X,avg}$ values are obtained from a catalogue of outbursting NSs (1). The $L_{\rm X,avg}$ values correspond to the average of $L_{\rm X,peak}$ values reached during each outburst, and $\dot{M}_{\rm avg} = L_{\rm X,avg} r_\star / G M_1$. The companion masses $M_{2,\rm min}$ are taken from the recently released catalogue of LMXBs, *XRBcats* [2] (2). In the seventh column we note some of the features of the sources (MS: main sequence, BD: brown dwarf, U: ultra-compact X-ray binaries, B: X-ray bursters, PRE: photospheric radius expansion observed during X-ray burst, GC: sources in globular clusters).

Name	$P_{\rm orb}$ (h)	P (ms)	d (kpc)	$L_{\rm X,avg}$ (erg s^{-1})	$\dot{M}_{\rm avg}$ (g s^{-1})	$M_{2,\rm min}$ ($M_\odot$)	Flags	References
Aql X-1	18.95	1.82	4.50	1.94×10^{37}	1.04×10^{17}	0.56	MS,B	(1), (2)
SWIFT J1749.4-2807	8.82	1.93	6.70	1.67×10^{36}	8.97×10^{15}	0.59	MS,B	(1), (2)
IGR J17591-2342	8.80	1.90	8.00	2.50×10^{36}	1.35×10^{16}	0.42	MS	(1), (2)
SAX J1748.9-2021	8.76	2.26	8.50	2.60×10^{37}	1.40×10^{17}	0.10	MS,B,GC	(1), (2)
SRGA J144459.2-604207	5.22	2.23	8.50	1.32×10^{37}	7.10×10^{16}	0.2 - 0.7	MS,B	(1), (2)
MAXI J1816-195	4.83	1.89	<6.3	1.50×10^{37}	8.07×10^{16}	0.55	MS,B	(1), (2)
XTE J1814-338	4.27	3.20	8.00	1.59×10^{36}	8.56×10^{15}	0.17	MS,B,PRE	(1), (2)
IGR J17498-2921	3.84	2.49	7.60	3.85×10^{36}	2.07×10^{16}	0.17	MS,B,PRE	(1), (2)
IGR J17511-3057	3.47	4.08	6.90	2.70×10^{36}	1.45×10^{16}	0.13	MS,B	(1), (2)
IGR J00291+5934	2.46	1.67	4.20	1.12×10^{36}	6.00×10^{15}	0.039	BD	(1), (2)
SAX J1808.4-3658	2.01	2.49	3.50	1.69×10^{36}	9.07×10^{15}	0.043	BD,B,PRE	(1), (2)
IGR J17379-3747	1.88	2.14	8.50	2.48×10^{36}	1.34×10^{16}	0.056	BD	(1), (2)
HETE J1900.1-2455	1.39	2.65	4.70	2.10×10^{36}	1.13×10^{16}	0.016	BD,B	(1), (2)
IGR J17494-3030	1.25	2.66	8.00	8.85×10^{35}	4.76×10^{15}	0.02	He WD?, U	(1), (2)
MAXI J1957 + 032	1.01	3.19	5.00	1.43×10^{36}	7.69×10^{15}	0.017	He WD?	(1), (2), (3)
NGC 6440 X-2	0.96	4.86	8.50	1.43×10^{36}	7.69×10^{15}	0.00067	He WD, U, GC	(1), (2)
SWIFT J1756.9-2508	0.91	5.49	8.00	2.78×10^{36}	1.49×10^{16}	0.007	He WD, U	(1), (2)
IGR J16597-3704	0.77	9.51	9.10	2.20×10^{36}	1.18×10^{16}	0.006	He WD, U,GC	(1), (2)
MAXI J0911-655	0.74	2.94	9.50	1.90×10^{36}	1.02×10^{16}	0.024	He WD?, U,GC	(1), (2)
XTE J0929-314	0.73	5.40	>6	6.24×10^{36}	3.36×10^{16}	0.0083	C/O WD, U	(1), (2)
XTE J1751-305	0.71	2.30	8.50	6.24×10^{36}	3.36×10^{16}	0.014	He WD, U	(1), (2)
XTE J1807-294	0.67	5.25	8.00	9.60×10^{36}	5.17×10^{16}	0.0066	C/O WD, U	(1), (2)
IGR J17062-6143	0.63	6.11	7.30	8.70×10^{35}	4.68×10^{15}	0.0006	He WD?, U,B	(1), (2)

Note. (1): C. O. Heinke et al. 2025, (2): A. Avakyan et al. 2023, (3) A. Sanna et al. 2022.

$P_{\rm orb} < 3$ h with $\langle P \rangle \simeq 2.5$ ms. The last group includes AMXPs in ultra-compact X-ray binaries (UCXBs) with $P_{\rm orb} < 80$ min. These are 10 sources with extremely low-mass ($M_2 \simeq 0.001\,M_\odot$) degenerate He/CO white dwarf (WD) companions. These systems with $\langle P \rangle \simeq 5.2$ ms spin relatively slowly compared to other AMXPs. The categorization of AMXPs into these three groups suggests distinct evolutionary paths for their LMXB progenitors. This has been suggested by C. J. Deloye (2008), who explored the evolutionary connections between LMXBs and RMSPs in close orbits. A critical aspect influencing these formation channels is the bifurcation period $P_{\rm bif}$. This is the value of $P_{\rm orb}$ at the onset of RLOF and is estimated to be $P_{\rm bif} \lesssim 1$ d (E. H. P. Pylyser & G. J. Savonije 1988, 1989). LMXBs with $P_{\rm orb} < P_{\rm bif}$ are converging systems, which evolve with decreasing $P_{\rm orb}$. In contrast, the binaries with $P_{\rm orb} > P_{\rm bif}$ are diverging systems evolving into wide-orbit systems with $P_{\rm orb} > 10$ d.

The evolutionary tracks for the AMXP groups with BD, He WD, and MS companions described above can be referred to as BD-track, UCXB-track, and MS-track. The details of these evolutionary tracks were investigated by X. He, X.-C. Meng & H.-L. Chen (2019), who successfully reproduced most of the binary and companion properties of AMXPs ($P_{\rm orb}$, M_2, and the X-ray luminosity L_X). Other studies have also investigated the evolution of binary and companion properties, as well as the formation of RMSPs, UCXBs, and other AMXPs (A. G. Istrate, T. M Tauris & N. Langer 2014; R. Sengar et al. 2017; T. M. Tauris 2018). Formation of AMXPs considering the evolution of both the binary and the individual properties of the two stars was first studied by A. Kar, P. Ojha & S. Bhattacharyya (2024). There are other recent works that studied the long-term evolution of LMXBs by integrating the spin evolution of the NS with a focus on the formation of RMSPs and spider pulsars, skipping the AMXP stage (S.-Y. Lan & X.-C. Meng 2023; D. Misra, K. I. Koljonen & M. Linares 2025a; D. Misra, M. Linares & C. S. Ye 2025b). In this work, we will use the stellar evolution code MODULES FOR EXPERIMENTS IN STELLAR ASTROPHYSICS (`mesa`, B. Paxton et al. 2011, 2013, 2015, 2018, 2019; A. S. Jermyn et al. 2023) to investigate the long-term evolution of LMXBs with initial orbital periods below or near $P_{\rm bif}$. These systems undergo long-lasting stable mass transfer, leading to the formation of AMXPs following three specific evolutionary tracks: BD-track, UCXB-track, and MS-track. For each of these evolutionary tracks, we will also study the rotational evolution of the NS using the analytical model developed by U. Ertan (2021).

The duration and stability of mass transfer from the companion to the RL of the NS depend significantly on the mechanisms of mass and angular momentum loss (AML). In LMXBs, AML is primarily driven by the gravitational radiation (GR) and magnetic braking (MB) (D. Bhattacharya & E. P. van den Heuvel 1991; T. M. Tauris & E. P. J. van den Heuvel 2023). The AML by GR is efficient particularly in tight-orbit systems like UCXBs during the late phases of evolution. Conversely, MB can efficiently drain the orbital angular momentum of the binary during the early phases of the evolution. MB occurs in Sun-like MS or dwarf stars with convective envelopes. As the donor star slows down, the angular momentum is carried away by a magnetically coupled stellar wind, with a negligible mass-loss (ML) of the donor star. Recent studies have shown that the conventional MB model, commonly referred to as the Skumanich law (A. Skumanich 1972; S. Rappaport et al.

1983), is not successful in reproducing some observed properties of LMXBs (K. Pavlovskii & N. Ivanova 2016). In particular, the mass transfer rates are underestimated by an order of magnitude with these conventional models (see K. X. Van, N. Ivanova & C. O. Heinke 2019, for details). Formation and evolution of accreting LMXBs were also investigated with different MB models (Z.-L. Deng et al. 2021; M. Echeveste et al. 2024; H.-R. Yang & X.-D. Li 2024). Z.-L. Deng et al. (2021) analysed the effect of MB prescription on both LMXB and RMSP stages, combining binary evolution and binary population synthesis. The results of this work indicate that the convection-boosted (τ- boosted) MB model proposed by K. X. Van et al. (2019) is a suitable MB model to study the long-term evolution of LMXBs. Based on these findings, we adopt the τ-boosted MB model to investigate the evolutionary tracks of AMXPs with `mesa` .

The analytical model employed in this work is based on the basic principles of the disc-field interaction model developed by R. V. E. Lovelace, M. M. Romanova & G. S. Bisnovatyi-Kogan (1999) and G. V. Ustyugova et al. (2006). In this model, the closed field lines that are interacting with the inner disc within a narrow boundary layer inflate, open up, and reconnect on the dynamical time-scale of the disc. The field lines are open and disconnected from the outer disc outside the interaction region. In the conventional models, the entire disc is assumed to be threaded by the closed field lines inside the light cylinder (P. Ghosh & F. K. Lamb 1979). However, it was shown in later work that the closed field lines rotating with the star cannot slip through the disc since the diffusion time-scale of the field lines is much longer than the interaction time-scale of the lines with the inner disc (S. Fromang & J. M. Stone 2009). At the inner disc radius, $r_{\rm in}$, the field lines should be sufficiently strong to force the matter into co-rotation within the short interaction time-scale. In the SP phase, all the inflowing matter can be thrown out of the system along the open field lines (see e.g. D. A. Uzdensky 2004). There is a maximum radius at which this SP mechanism can work, which is likely to be close to the actual $r_{\rm in}$. U. Ertan (2017) estimated this $r_{\rm in}$ through analytical calculations as a function of P, $\dot{M}_{\rm in}$, and the magnetic dipole moment μ, and found that it is much smaller than the conventional Alfvén radius, $r_{\rm A}$, in this phase. The model was later extended to calculate $r_{\rm in}$ and the torques in all rotational phases [SP, weak propeller (WP), and spin-up (SU)], as well as the critical conditions for the transitions between these phases (U. Ertan 2021).

Conventional models, which assume the inner disc radius to be close to $r_{\rm A}$, cannot account for some typical properties of LMXBs. These include ongoing accretion at low $L_{\rm X}$ levels while the NS spins down, as well as torque reversals occurring with small changes in $L_{\rm X}$ and with comparable torque magnitudes on either side of the reversal (for a review see L. Bildsten et al. 1997). Applications of the model of U. Ertan (2017, 2021) to different classes of LMXBs yielded results that are consistent with observations. As a strongly magnetized system, the torque reversals of 4U 1626-67 were studied by A. A. Gençali et al. (2022). In weakly magnetized systems, the model was applied to investigate the SP/WP transitions of tMSPs (U. Ertan 2018) and to explain the lack of X-ray pulsations from most LMXBs, while a small fraction exhibit X-ray pulsations as AMXPs (N. Niang et al. 2024).

During the long-term evolution, the torques acting on the NS depend sensitively on both $\dot{M}_{\rm in}$ and $r_{\rm in}$. A. Kar et al. (2024) provided a comprehensive study of the long-term evolution of AMXPs. They reported that reproducing the observed spin frequencies of the fast-spinning AMXPs ($P \lesssim 3$ ms) with degenerate WD/BD companions remains challenging, and suggested that this problem could be resolved by considering the effects of transient accretion. We also use `mesa` for the binary evolution and obtain $\dot{M}_{\rm in}$ histories similar to those in A. Kar et al. (2024). The fact that our simulations can reproduce the properties of these fast rotating AMXPs indicates that the basic reason leading to different fast-spinning NS properties between the two analyses is the difference in the employed torque models together with $r_{\rm in}$ calculations. We adopt the analytical model developed by U. Ertan (2021), whereas A. Kar et al. (2024) used the torque model of S. Bhattacharyya & D. Chakrabarty (2017).

In this work, our aim is to investigate the binary evolution of LMXBs together with the rotational evolution of their NSs until the sources reach their equilibrium spin periods. For these calculations, we will use `mesa` to study the details of the evolutionary paths of AMXPs (BD-track, UCXB-track, and MS-track) and obtain the evolution of their donor's long-term mass transfer rate $\dot{M}_2$. Using the $\dot{M}_2$ histories estimated by `mesa` simulations, we will study the rotational evolution of the NS using the aforementioned analytical model. The evolution of the binary and donor properties ($P_{\rm orb}$, M_2, and $\dot{M}_2$) for each track is described in Section 2. We briefly describe the analytical model together with the illustrative long-term rotational evolutions of the NS (evolution of P and $\dot{P}$) evolving along each track in Section 3. We apply our results to selected individual AMXPs from the three evolutionary tracks in Section 4. These sources, namely HETE J1900.1-2455 for the BD-track, XTE J1751-305 for the UCXB-track, and Aql X-1 for the MS-track, have been observed over a long period and/or throughout multiple outbursts. We discuss our results in Section 5 and summarize our conclusions in Section 6.

2 PHYSICAL ASSUMPTIONS AND NUMERICAL SET-UP FOR THE BINARY EVOLUTION

2.1 Angular momentum loss mechanisms

We calculate the rate of orbital AML $\dot{J}_{\rm orb}$ as

$$\frac{\dot{J}_{\rm orb}}{J_{\rm orb}} = \frac{\dot{J}_{\rm ML}}{J_{\rm orb}} + \frac{\dot{J}_{\rm GR}}{J_{\rm orb}} + \frac{\dot{J}_{\rm MB}}{J_{\rm orb}}, \tag{1}$$

where the terms on the right-hand side of this equation represent the orbital AML mechanisms by means of ML, GR, and MB, respectively.

Mass-loss from the binary system

The orbital AML due to ML is commonly given as

$$\frac{\dot{J}_{\rm ML}}{J_{\rm orb}} = \frac{\alpha + \beta q^2 + \delta\gamma(1+q^2)}{1+q}\frac{\dot{M}_2}{M_2}\ {\rm s}^{-1} \tag{2}$$

(T. M. Tauris & E. P. J. van den Heuvel 2023), where α is the coefficient for ML through wind from the companion, β[1] determines the fraction of matter ejected from the vicinity of the NS (isotropic re-emission model, D. Bhattacharya & E. P. van den Heuvel 1991), δ is the coefficient for ML from a circumbinary coplanar disc with radius $a_{\rm r} = \gamma^2 a$, where a is the orbital separation. $q = M_2/M_1$, M_1 is the NS mass, and $\dot{M}_2$ is the mass-transfer

[1]We note that this definition of β differs from the one used among binary modelling works (e.g. P. Podsiadlowski, S. Rappaport & E. D. Pfahl 2002).

rate of the donor. The ML through the wind is negligible and there is no circumbinary disc around these systems; therefore we take $\alpha = \delta = 0$. Equation (2) then reduces to

$$\frac{\dot{J}_{\rm ML}}{J_{\rm orb}} = \beta \, \frac{q^2}{1+q} \, \frac{\dot{M}_2}{M_2} \, {\rm s}^{-1} \tag{3}$$

The accretion efficiency given by $\epsilon = 1 - \alpha - \beta - \delta$ reduces to $\epsilon = 1 - \beta$. As a result, the mass-transfer rate on to the NS is $\dot{M}_1 = \epsilon \, |\dot{M}_2|$.

Gravitational radiation

The orbital AML due to GR can be written as

$$\frac{\dot{J}_{\rm GR}}{J_{\rm orb}} = -\frac{32}{5\,c^5} \, \frac{G^3 M_1 \, M_2 \, (M_1 + M_2)}{a^4} \, {\rm s}^{-1} \tag{4}$$

(J. Faulkner 1971), where G is the gravitational constant and c is the speed of light. In close-orbit systems ($P_{\rm orb} < 6$ h), which have degenerate companion stars, GR is the dominant AML mechanism due to the a^{-4} dependence in equation (4). LMXBs in which GR is the dominant torque correspond to systems with $P_{\rm orb} < P_{\rm bif}$ that are in an advanced phase of evolution. As GR is not effective during the early stages of the evolution, there must be another torque that drains the angular momentum of the system, which is linked to the MB of the companion star.

Magnetic braking

In close binaries ($P_{\rm orb} < 3$ d), the angular momentum lost by the companion is replenished at the expense of the orbital angular momentum of the binary through tidal interactions (T. M. Tauris & E. P. J. van den Heuvel 2023). As a result, the donor star is forced to fill its RL and initiate mass transfer. The AML by MB is conventionally calculated as

$$\frac{\dot{J}_{\rm MB,Sk}}{J_{\rm orb}} = -3.8 \times 10^{-30} \, f \, \frac{{R_\odot}^4 \, (R_2/R_\odot)^{\gamma_{\rm MB}} \, G(M_1 + M_2)^2}{a^5 \, M_1} \, {\rm s}^{-1}, \tag{5}$$

where R_2 is the donor star radius, $\gamma_{\rm MB}$ is the MB index ($\gamma_{\rm MB} \simeq 2 - 5$), and $f = 0.73$ (A. Skumanich 1972). Equation (5) is also known as the Skumanich law (S. Rappaport et al. 1983). The conventional MB prescription underestimates the $\dot{M}_2$ of LMXBs by an order of magnitude (P. Podsiadlowski et al. 2002; K. Pavlovskii & N. Ivanova 2016). To remedy this discrepancy, a modified MB model has been proposed by K. Pavlovskii & N. Ivanova (2016) and was later extended in the works of K. X. Van et al. (2019) (hereafter VIH19) and K. X. Van & N. Ivanova (2019, 2021). In the Skumanich law, the AML due to MB depends on M_2, R_2, and the rotational rate of the companion star Ω_2 as $\dot{J}_{\rm MB,Sk} \propto M_2 \, R_2^{\gamma_{\rm MB}} \, \Omega_2^3$. Assuming isotropic isothermal winds, a radial magnetic field and a rotational boost of the magnetic field, VIH19 obtained an MB torque that scales the same as the Skumanich law. The VIH19 MB model considers an additional scaling of MB with the wind ML rate of the companion, together with a scaling of the magnetic field strength with the turnover time of convective eddies. The general form of the VIH19 MB law is given as

$$\dot{J}_{\rm MB,\,boost} = \dot{J}_{\rm MB,Sk} \left(\frac{\Omega_2}{\Omega_\odot}\right)^{\beta_{\rm boost}} \left(\frac{\tau_{\rm conv}}{\tau_{\odot,\,\rm conv}}\right)^{\xi_{\rm boost}} \left(\frac{\dot{M}_{2,\rm W}}{\dot{\rm M}_{\odot,\rm W}}\right)^{\alpha_{\rm boost}}, \tag{6}$$

where $\Omega_\odot \approx 3 \times 10^{-6}$ s^{-1} is the angular frequency of the Sun, $\tau_{\rm conv}$ is the turnover time of convective eddies, $\tau_{\odot,\,\rm conv} = 2.8 \times 10^6$ s (see K. X. Van et al. 2019, for details), $\dot{M}_{2,\rm W} = 2.52 \times 10^{13} \left(\frac{R_2}{R_\odot}\right) \left(\frac{L_2}{L_\odot}\right) \left(\frac{M_\odot}{M_2}\right)$ g s^{-1} is the wind ML rate of the companion, and L_2 is the luminosity of the companion (D. Reimers 1975). Depending on the values of ($\beta_{\rm boost}$,$\xi_{\rm boost}$,$\alpha_{\rm boost}$), there are four cases considered in the VIH19 MB law: default (0,0,0), convection-boosted (τ- boosted) (0,2,0), intermediate (0,2,1) and wind-boosted (2,4,1). Using `mesa`, VIH19 simulated 2136 binaries for each of the four cases to compare the impact of these prescriptions against known LMXB populations. While the intermediate MB model is better at reproducing the properties of observed LMXBs, the τ-boosted MB also yields results in good agreement with observations. Independent support for the τ-boosted model was later provided by Z.-L. Deng et al. (2021), who combined detailed binary evolution with binary population synthesis across both the LMXB and RMSP stages. Motivated by these results, we adopt the τ-boosted model, which can be written as

$$\frac{\dot{J}_{\rm MB}}{J_{\rm orb}} = \frac{\dot{J}_{\rm MB,Sk}}{J_{\rm orb}} \left(\frac{\tau_{\rm conv}}{\tau_{\odot,\,\rm conv}}\right)^2 \tag{7}$$

2.2 Physical assumptions

There are ~ 190 LMXBs hosting NSs that have been observed with $L_{\rm X}$ varying between 10^{31} and 10^{38} erg s^{-1}. Sources with $L_{\rm X} < 10^{35}$ erg s^{-1} are mostly transient and in quiescence, while those with $10^{35} < L_{\rm X} < 10^{38}$ erg s^{-1} are either transient sources in their outburst states or persistent sources (for details, see A. Bahramian & N. Degenaar 2022). There is a critical mass accretion rate, $\dot{M}_{\rm crit}$, that depends on $P_{\rm orb}$, below which the accretion disc becomes viscously unstable. Below this threshold ($\dot{M}_1 < \dot{M}_{\rm crit}$), the system becomes a transient source that shows cyclic outbursts with durations from a few weeks to several months and recurrence times varying from a few months to several years, indicating that the transient sources are predominantly in their quiescent states (for details of disc instability model see e.g. G. Dubus et al. 1999; J. P. Lasota 2001). All known AMXPs are transient sources. Among these systems, some sources like HETE J1900.1-2455 and MAXI J0911-655 exhibited extended outburst phases lasting up to 7 yr. We adopt the $\dot{M}_{\rm crit}$ as estimated by G. Dubus et al. (1999), given by the relation

$$\dot{M}_{\rm crit} = 2.36 \times 10^{15} \left(\frac{M_1}{1.4\,{\rm M}_\odot}\right)^{1/2} \left(\frac{M_2}{\rm M_\odot}\right)^{-1/5} \left(\frac{P_{\rm orb}}{\rm h}\right)^{7/5} {\rm g\,s^{-1}} \tag{8}$$

The mass accretion rate on to the NS, $\dot{M}_1$, is assumed to be Eddington limited, which is given in VIH19 as

$$\dot{M}_{\rm Edd} \approx 2.14 \times 10^{18} \frac{1}{1+X} \, {\rm g\,s^{-1}}, \tag{9}$$

where X is the hydrogen mass fraction in the material transferred from the donor.

2.3 Input physics and initial conditions

To obtain the evolutionary tracks of AMXPs, we used the 1D stellar evolution code `mesa` , version 11701 (B. Paxton et al. 2011, 2013, 2015, 2018, 2019). In all the simulations, the NS is considered as a point mass evolving with a zero-age main sequence companion with metallicity $Z = 0.02$. We treat convection according to the Schwarzschild criterion with a mixing length parameter of $\alpha_{\rm MLT} = 2.0$ and account for thermohaline mixing with a coefficient $\alpha_{\rm th} = 1.0$. We allow wind ML of the donor via a Reimers-type wind. We chose $M_{1,\rm i} = 1.4\,{\rm M}_\odot$ and $M_{2,\rm i} = 1.1\,{\rm M}_\odot$

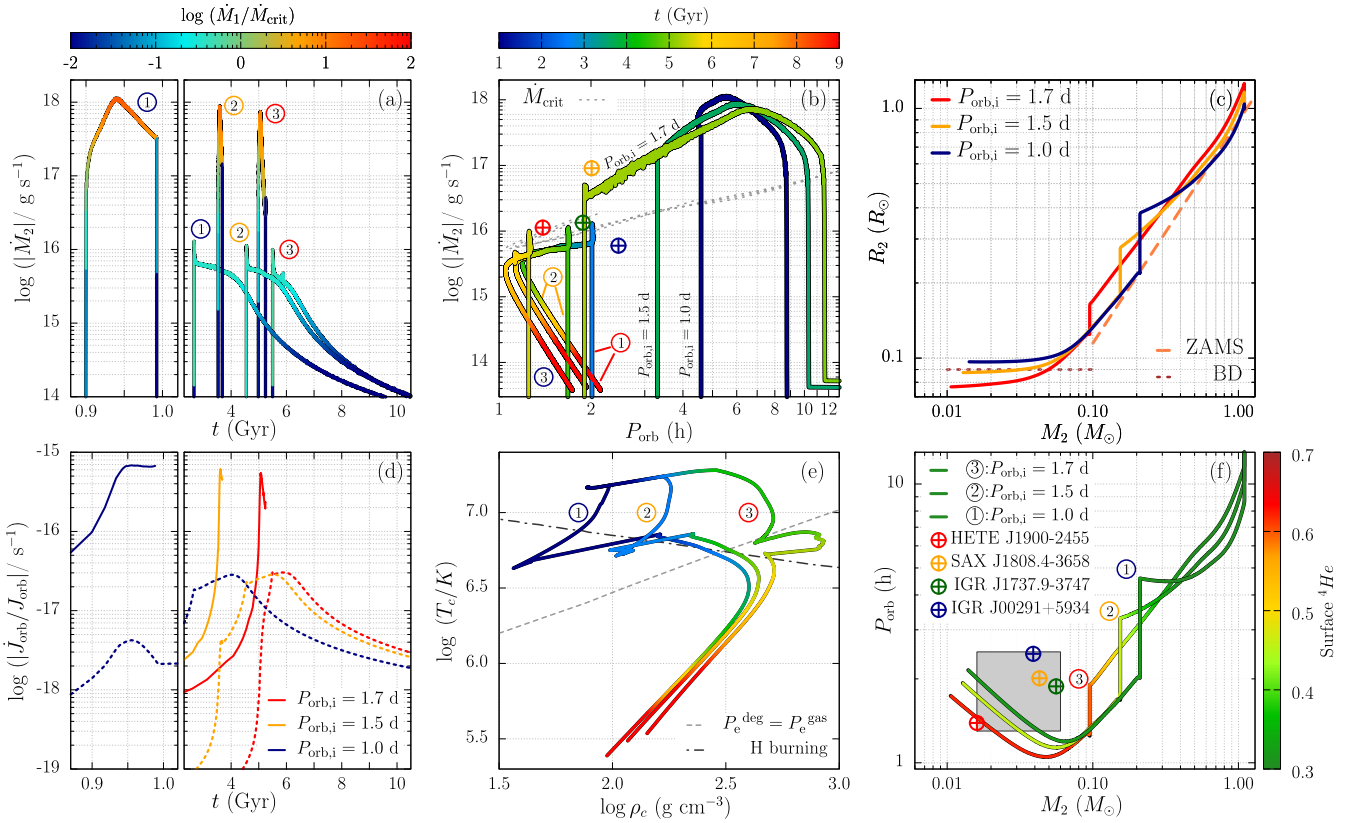

Figure 1. Illustrative model tracks representing LMXBs evolving along the BD-track obtained with $P_{\rm orb,i} = 1.0$ (curve 1), 1.5 (curve 2), and 1.7 (curve 3) d. For the three model sources, $M_{1,\rm i} = 1.4\,{\rm M}_\odot$, $M_{2,\rm i} = 1.1\,{\rm M}_\odot$, and $\gamma_{\rm MB} = 3$. (a) and (b) show the evolution of $\dot{M}_2$ as a function of time and $P_{\rm orb}$, respectively. The colour bar in (a) and (b) indicates the $\dot{M}_{1/\dot{M}_{\rm crit}}$ to distinguish the persistent and transient phases of the evolution and the time, respectively. The dashed curve in (b) is $\dot{M}_{\rm crit}$. The symbols '⊕' show AMXPs with BD companions given in Table 1. (c) Evolution of R_2 as a function of M_2. (d) Evolution of the AML rates $\dot{J}_{\rm MB}$ (solid lines) and $\dot{J}_{\rm GR}$ (dashed lines). (e) Evolution of the companion in the temperature–central density ($T_{\rm c}$–$\rho_{\rm c}$) plane. The dashed line represents the border between the degenerate matter (below the line) and the non-degenerate matter (above the line) and the dot–dashed line is the critical line for the hydrogen burning. (f) Evolution of $P_{\rm orb}$ as a function of M_2 with the colour bar indicating the donor's surface abundance in helium. The grey area indicates the regions in which this subgroup of AMXPs are observed.

as canonical values where $M_{1,\rm i}$ is the initial NS mass and $M_{2,\rm i}$ is the initial donor mass. Since we are interested in evolutionary tracks evolving to AMXPs (convergent systems), we chose initial orbital period values $P_{\rm orb,i} < 3$ d. We choose $\beta = 0.5$ and $\gamma_{\rm MB} = 3$ as canonical values and discuss the impact of different values of β and $\gamma_{\rm MB}$ in Section 2.5. We note that our results are not very sensitive to q, $\gamma_{\rm MB}$, and β. With different values of these parameters, similar evolutionary tracks can be obtained with small adjustments to $P_{\rm orb,i}$ (see Section 2.5).

2.4 The evolutionary tracks of AMXPs

Here we present the results of our simulations with the `mesa` code that can reproduce the three evolutionary tracks of AMXPs. We obtain these illustrative evolutionary tracks, changing only the $P_{\rm orb,i}$ parameter of the model binaries in the ranges of 1.0–2.0 d for BD-tracks, 1.7–3.0 d for UCXB-tracks, and 1.2–3.0 d for MS-tracks. All other parameters described above (given in the figure captions) are held constant throughout these simulations. Each track is evaluated against four key criteria that must be met simultaneously within a Hubble time to be counted as an evolutionary path for AMXPs: (i) The system must enter a transient regime towards the end of its evolution; (ii) the final values of M_2 and $P_{\rm orb}$ must fall within the observed ranges specific to each group of AMXPs; (iii) the surface composition should be relatively hydrogen-rich for AMXPs with MS and BD companions, and helium-rich for those with He WD companions; (iv) the mass and radius of the donor star must correspond to those of the observed donor types in AMXPs.

The results for the model binaries are illustrated in Figs 1–3, showing the evolution of binary properties ($\dot{J}_{\rm orb}/J_{\rm orb}$ and $P_{\rm orb}$) and donor properties (M_2, R_2, and $\dot{M}_2$). To assess the validity of our evolutionary tracks for different groups of AMXPs, we plot these tracks alongside actual AMXPs on the $P_{\rm orb}$–$\dot{M}_2$ and M_2–$P_{\rm orb}$ planes (panels b and e in Figs 1–3). We summarize the details for each track in the following text.

2.4.1 *The BD-track*

AMXPs with BD companions have 1 h $< P_{\rm orb} <$ 3 h and $M_2 \simeq 0.01\,{\rm M}_\odot$. For an MS donor to evolve to a BD star within Hubble time, the mass transfer must be initiated on a time-scale shorter than the nuclear time-scale, $\tau_{\rm nuc}$, before the companion burns a significant fraction of its core hydrogen to helium. This condition is satisfied for 0.5 d $< P_{\rm orb,i} <$ 1.7 d. It is seen in Figs 1(a) and (d) that the three model binaries have the same $\dot{M}_2(t)$ and $\dot{J}_{\rm orb}(t)$ morphologies.

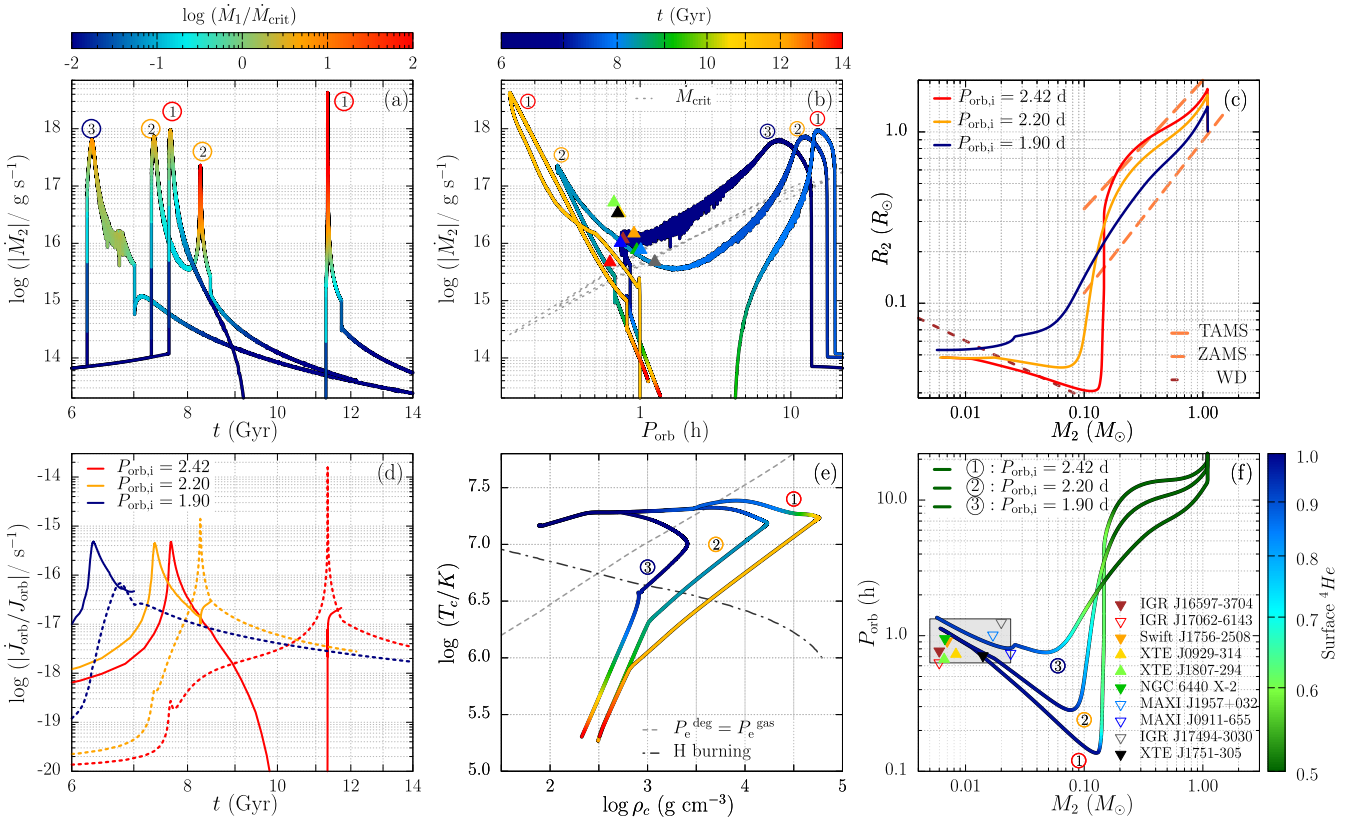

Figure 2. Same as Fig. 1. These illustrative model tracks that can represent typical UCXB evolutions are obtained with $P_{\rm orb,i} = 2.42$ d (curve 1), 2.20 d (curve 2), and 1.90 d (curve 3). The '▼' signs show observed AMXPs with He WD companions, the '▲' signs are observed AMXPs with C/O WD companions and the '▽' signs represent observed AMXPs in UCXBs with some uncertainty in the companion type.

For $P_{\rm orb,i} = 1.0$ d, the orbital separation decreases due to AML via MB. In this phase, the MB strength reaches a maximum and the RL radius cannot increase fast enough and the mass transfer via RLOF is initiated when $P_{\rm orb} = P_{\rm RLOF} \simeq 9$ h, where $P_{\rm RLOF}$ is the value of $P_{\rm orb}$ at the onset of RLOF, and $\dot{M}_2 \sim 10^{18}$ g s^{-1} ($\dot{M}_2 > \dot{M}_{\rm crit}$, the system is persistently accreting). The initial $\dot{M}_2$ depends on the chosen MB model and the value of $P_{\rm RLOF}$, which also depends on the chosen MB model (see the discussion in Z.-L. Deng et al. 2021; H.-R. Yang & X.-D. Li 2024). Indeed, for similar parameters, initial $\dot{M}_2$ is a few times greater with the conventional Skumanich MB model. As the strength of the MB torques decreases, $\dot{M}_2$ decreases below $\dot{M}_{\rm crit}$ and the system enters the transient regime (see Fig. 1a). The donor star becomes fully convective during the early stage of mass transfer inactivating the MB torques. At this stage ($P_{\rm orb} < 3$ h), the donor has transferred nearly 90 per cent of its mass. During the RLOF, the donor shrinks due to the ML (see Fig. 1c). The RL radius cannot readjust fast enough within the thermal time-scale and the RLOF terminates until the relatively weak GR torques reduce the orbital separation and initiate a second RLOF phase when $t \sim 3$ Gyr. The correlation between $\dot{M}_2$ and the torques acting on the binary can be seen in Figs 1(a) and (d). GR torques are dominant in close binary systems ($P_{\rm orb} < 3$ h), and strong enough to drive the system into another RLOF phase during which the system evolves as a transient source ($\dot{M}_2 \sim 10^{15}$ g s^{-1} $< \dot{M}_{\rm crit}$). The donor becomes fully degenerate when it moves below the theoretical line that separates non-degenerate matter and degenerate matter at $t \sim 5$ Gyr (see dashed line in Fig. 1e). The donor evolves towards the BD region when $M_2 \sim 0.05\,{\rm M}_\odot$. The mass–radius relation of the donor corresponds to that of BD ($R_2 \propto 0.1 M_2$ for $M_2 < 0.1 M_\odot$; A. A. Zdziarski et al. 2016) (see Fig. 1c). When the evolution terminates at $t \sim 14$ Gyr, $P_{\rm orb} \sim 2$ h, and $M_2 \sim 0.014\,{\rm M}_\odot$. At this time, the surface helium abundance of the donor is ~ 32 per cent. This is due to the onset of RLOF during the early phases of nuclear burning. Consequently, the change in surface helium abundance is negligible compared to models with larger $P_{\rm orb,i}$, where the abundance increases significantly as the donor evolves (see Figs 1e and f).

For the other model binaries, $P_{\rm RLOF} \simeq 10$ h for $P_{\rm orb,i} = 1.5$ d and $P_{\rm RLOF} \simeq 12$ h for $P_{\rm orb,i} = 1.7$ d. We observe that for given $M_{1,\rm i}$ and $M_{2,\rm i}$ values, $P_{\rm RLOF}$ increases with increasing $P_{\rm orb,i}$, a measure of orbital separation, since the RL radius is proportional to the orbital separation (P. P. Eggleton 1983). In each case, $\dot{M}_2$ is similar but slightly smaller compared to the $\dot{M}_2$ of the model with $P_{\rm orb,i} = 1.0$ d. This is due to the slight difference in strength of MB at the beginning of mass transfer, which decreases with $P_{\rm orb,i}$ (see Figs 1a and d). The duration of the initial RLOF increases with increasing $P_{\rm orb,i}$ (~ 0.2 Gyr for $P_{\rm orb,i} = 1.5$ d and ~ 0.3 Gyr for $P_{\rm orb,i} = 1.7$ d). As a result, the final donor mass is also smaller for greater $P_{\rm orb,i}$ ($M_2 \simeq 0.012$ M$_\odot$ for $P_{\rm orb,i} = 1.5$ d and $M_2 \simeq 0.010$ M$_\odot$ for $P_{\rm orb,i} = 1.7$ d; see Fig. 1c). The second RLOF is initiated at $t \sim 5$ Gyr for $P_{\rm orb,i} = 1.5$ d and $t \sim 6$ Gyr for $P_{\rm orb,i} = 1.7$ d. Nuclear burning of the donor also lasts longer for binaries with greater $P_{\rm orb,i}$. This leads to a higher surface helium

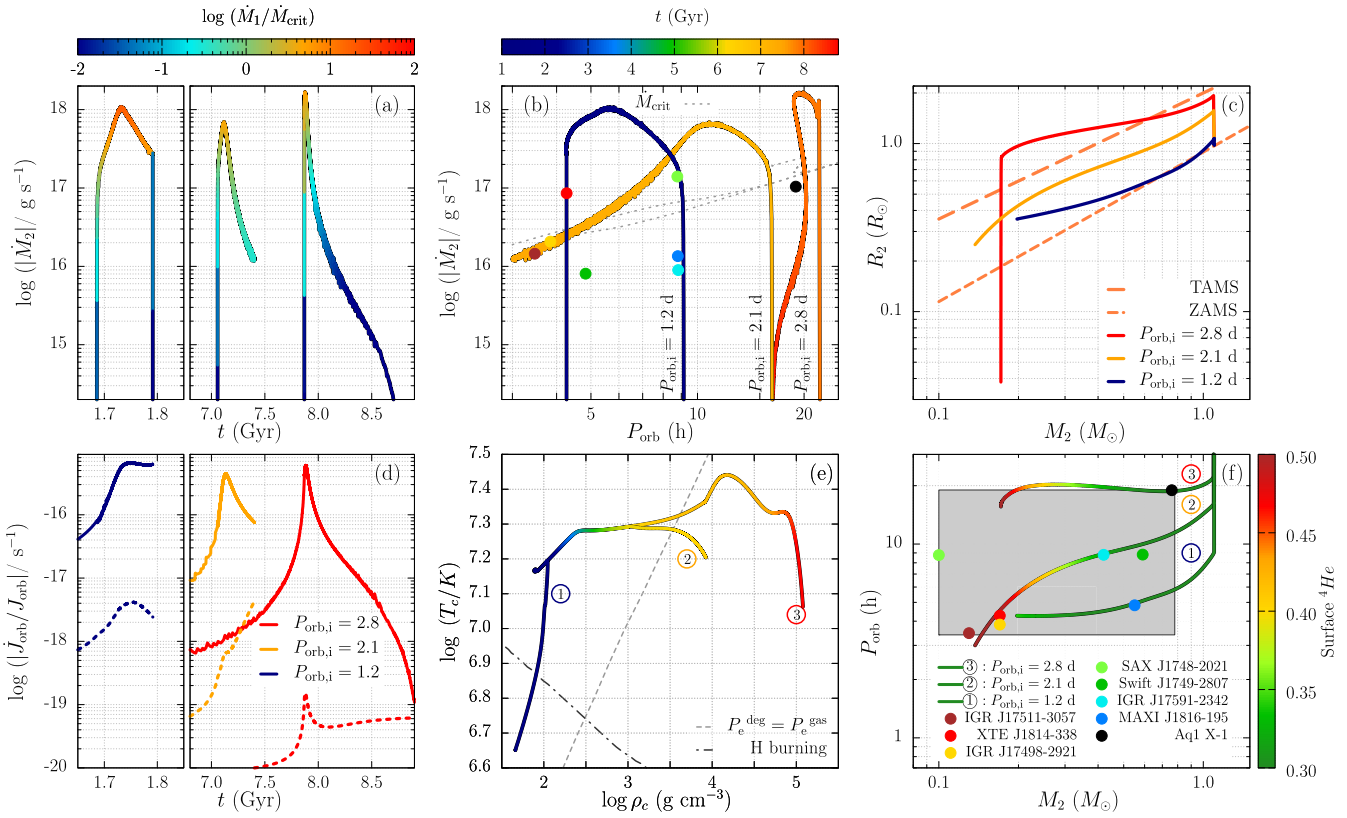

Figure 3. Same as Fig. 1. These model curves that can represent the evolution of AMXPs with MS companion are obtained with $P_{\rm orb,i} = 2.8$, 2.1, and 1.2 d. The filled circles show observed AMXPs with MS companions.

abundance of the donor by the end of its evolution (~ 45 per cent for $P_{\rm orb,i} = 1.5$ d and ~ 60 per cent for $P_{\rm orb,i} = 1.7$ d).

We plotted the AMXPs with BD donors on the M_2–$P_{\rm orb}$ plane alongside three model binary systems with $P_{\rm orb,i} = 1.0$, 1.5, and 1.7 d, respectively (see Fig. 1e). The observed $P_{\rm orb}$ and M_2 of the source HETE J1900.1 − 2455 can be reproduced on the BD-track with $P_{\rm orb,i} = 1.7$ d, which is in agreement with observations. We could not find evolutionary tracks that match the observed properties of the remaining sources SAX J1808.4-3658, IGR J00291+5934, and MAXI J1957+032 on the M_2–$P_{\rm orb}$ plane. These sources have observed $P_{\rm orb}$ values slightly larger than those predicted by our evolutionary tracks. Studies of the formation and evolution of spider pulsars indicate that the black widow pulsars share similarities with AMXPs with BD donors (H. L. Chen et al. 2013; W. C. Chen 2017). Indeed, they have similar observed M_2 and $P_{\rm orb}$, while black widows have relatively higher $P_{\rm orb}$. This orbital expansion is likely caused by the irradiation of the companion by the NS as it spins down between mass transfer phases. The spin-down luminosity of the NS irradiates the companion, causing its evaporation through a stellar wind, which results in orbital expansion (H. L. Chen et al. 2013; D. Misra et al. 2025b). This irradiation effect is not addressed in our binary models, which is likely to be the reason our analysis could not accurately reproduce the properties of SAX J1808.4-3658, IGR J00291+5934, and MAXI J1957+032 on the M_2–$P_{\rm orb}$ plane.

We plot the same sources on the $P_{\rm orb}$–$\dot{M}_2$ plane together with three model binaries with $P_{\rm orb,i} = 1.0$, 1.5, and 1.7 d, respectively (see Fig. 1b). The grey dashed lines correspond to $\dot{M}_{\rm crit}$. To plot the AMXPs with BD donors, we use $\dot{M}_2 = \dot{M}_{\rm avg}$, where $\dot{M}_{\rm avg}$ corresponds to values seen in Table 1. Here, $L_{\rm X,avg}$ represents the average peak luminosities of the sources observed during outbursts (C. O. Heinke et al. 2025). As seen in Fig. 1(b), the four sources remain above the $\dot{M}_{\rm crit}$ line (while IGR J00291+5934 is close to but below the line). Furthermore, our model tracks indicate that these sources are close to the onset of the second accretion phase. Most of these systems are likely to have completed their SU phase.

2.4.2 *The UCXB-track*

UCXBs are systems with observed $P_{\rm orb} < 80$ min and an extremely low-mass degenerate donor He/CO WD with $M_2 \simeq 0.001\,{\rm M}_\odot$. Model binaries for UCXB-tracks can be obtained with 1.7 d $< P_{\rm orb,i} <$ 3.0 d (Fig. 2). The model BD-tracks in Fig. 1 are sensitive to the chosen $P_{\rm orb,i}$ and show similar morphology. However, the UCXB model tracks we obtain, which are also sensitive to the chosen $P_{\rm orb,i}$, do not exhibit the same morphology. We distinguish three different cases, which are summarized below.

The evolution of the model source with $P_{\rm orb,i} \simeq 2.42$ d represents Case 1 in Fig. 2, the donor evolves on $\tau_{\rm nuc}$ and burns most of its core hydrogen before initiating mass transfer at around the terminal-age main sequence (TAMS) at $t \sim 7.5$ Gyr. The orbital separation decreases due to AML via MB, and the RLOF starts with a rate rapidly increasing to $\dot{M}_2 \sim 10^{18}$ g s^{-1} when $P_{\rm orb} \simeq 20$ h. During this stage, the MB torque is at its strongest level. With decreasing strength of MB torques, and thus $\dot{M}_2$, the system enters a transient regime (see Fig. 2). Around $P_{\rm orb} \sim 4$ h, the donor evolves away from the TAMS. After ~ 90 per cent of its mass was transferred, the donor can no longer fill its RL, the RLOF phase terminates switching off the LMXB phase. $P_{\rm orb}$

continues to decrease to ~ 1 h while both MB and GR torques are active. During this time interval that lasts ~ 2.0 Gyr, the source is not detectable as an X-ray source, while it could be observed as an RMSP (R. Sengar et al. 2017; T. M. Tauris 2018). This time interval increases with increasing $P_{\rm orb,i}$ (e.g. ~ 3.5 Gyr for $P_{\rm orb,i} \sim 2.5$ d). With increasing strength of the GR torques, the orbital separation continues to decrease and finally initiates a second RLOF when $P_{\rm orb} \sim 1$ h. The donor is now a fully degenerate WD (see Figs 2c and e), and is able to refill its RL. Since the radius of a degenerate WD increases with decreasing mass ($R_{\rm WD} = 0.013\,R_\odot\,(M_{\rm WD}/M_\odot)^{-1/3}$, R. Sengar et al. 2017), the donor responds to ML by expanding. The resultant UCXB phase begins with $\dot{M}_2 \sim \dot{M}_{\rm Edd}$ with persistent accretion. The orbital separation continues to decrease until $P_{\rm orb}$ reaches a minimum around 10 min. The $\dot{M}_2$–$P_{\rm orb}$ correlation during the UCXB has been studied by R. Sengar et al. (2017), who showed that, towards the end of the evolution, all UCXB-tracks follow a common *declining* branch during which the orbit expands. Most of the remaining hydrogen envelope of the companion is accreted during the UCXB phase. The evolution ends with a transiently accreting NS, and a He WD donor with $M_2 \simeq 0.006\,{\rm M}_\odot$ and surface helium abundance of 98 per cent (see Figs 2b and f).

For Case 2 ($P_{\rm orb,i} = 2.20$ d), the initial steps of the evolution (LMXB phase) are rather similar to Case 1, with $P_{\rm RLOF} \simeq 17$ h. With a relatively shorter orbital separation, the GR torques are comparable to the MB torques at an earlier stage of the LMXB phase. As a result, the system enters into a transient regime during which $\dot{M}_2$ decreases and reaches a minimum $\sim 3 \times 10^{15}$ g s^{-1}. As the strength of the GR torques increases, $\dot{M}_2$ starts to increase, and the UCXB phase begins with persistent accretion (see Figs 2a and d). The evolution terminates similar to Case 1, when the surface helium abundance of the donor is about 98 per cent. Note that the detached phase encountered in Case 1, while the source could be observed as an RMSP, is not present in Case 2.

Case 3 ($P_{\rm orb,i} = 1.90$ d) can be considered as an extreme case of the BD-track with a greater value of $P_{\rm RLOF} \simeq 14$ h. Unlike Case 1 and Case 2, MB torques become negligible when the donor becomes degenerate (see Figs 2d and e). Afterwards, RLOF is maintained by the GR torques. The system evolves in the transient regime for the remainder of its lifetime, which ends when the companion has ~ 92 per cent surface helium abundance.

In Fig. 2(f), the AMXPs with He WD donors are plotted on the $M_2 - P_{\rm orb}$ plane alongside three illustrative model binary systems with $P_{\rm orb,i} = 2.42$, 2.00, and 1.90 d. These model curves are consistent with the observed M_2 and $P_{\rm orb}$ values of most AMXPs with He WD donors. However, XTE J0929-314 and XTE J1807-294, which host low-mass C/O WD companions, are likely to have evolved from intermediate mass X-ray binaries with $M_{2,\rm i} \geq 1.5$ M$_\odot$, a parameter range that was not explored in our analysis. The same sources and model tracks are also shown on the $P_{\rm orb} - \dot{M}_2$ plane in Fig. 2(b). These sources are typically located near the terminal stages of the model tracks. This indicates that the obtained model tracks are indeed representative of AMXPs with He WD companions.

2.4.3 The MS-track

AMXPs with MS companions have 3 h$< P_{\rm orb} <$ 19 h and $0.1\,{\rm M}_\odot < M_2 < 0.5\,{\rm M}_\odot$. Our results imply that these systems are likely to be observed at an early stage of their evolution on either BD or UCXB tracks. To illustrate this, we present one BD-track with $P_{\rm orb,i} = 1.2$ d and two UCXB-tracks with $P_{\rm orb,i} = 2.1$ d and $P_{\rm orb,i} = 2.8$ d in Fig. 3. We run these simulations until $P_{\rm orb} = 3$ h and/or $M_2 = 0.1\,{\rm M}_\odot$.

The UCXB-tracks described in Section 2.4.2 include two different long-term phases of accretion: an LMXB phase that is driven by MB torques during the early stage of the evolution and a UCXB phase that is driven by the GR torques, during the late stage of the evolution. For some systems, GR torques may not become strong enough to evolve into a UCXB phase. In such cases, the evolution terminates right after the LMXB phase. These 'pre-matured' UCXB-tracks terminate with properties similar to those of AMXPs with evolved MS companions. For these evolutionary paths, GR torques remain weaker than MB torques by an order of magnitude as the MB torques decrease. The pre-matured UCXB-tracks can be obtained with $P_{\rm orb,i}$ values in the range of 2.5 d $\lesssim P_{\rm orb,i} \lesssim$ 3.0 d, which lead to convergent systems.

For the model source shown in Fig. 3 with $P_{\rm orb,i} \sim 67$ h (2.8 d), the donor star evolves on $\tau_{\rm nuc}$, and approaches the TAMS before the mass transfer is initiated at $t \sim 8$ Gyr. The AML via MB gradually reduces the orbital separation, and RLOF starts when the $P_{\rm orb}$ decreases to $\simeq 22$ h. During this phase, the MB torques reach maximum strength, the resultant decrease in the size of the RL initiates a rapid ML at a rate of $\dot{M}_2 \sim 10^{18}$ g s^{-1}. Since the MB torques remain weak and the GR torques become even weaker, the orbital separation does not decrease significantly. Decreasing $\dot{M}_2$ takes the system into the transient regime (see Figs 3a and d). This occurs when the donor has transferred ~ 80 per cent of its mass, and $\dot{M}_2$ decreases below 10^{16} g s^{-1}. RLOF terminates at $t \sim 8.5$ Gyr, while ML via wind continues with rates $< 10^{14}$ g s^{-1}, without a significant effect on the binary evolution. We neglect the contributions of winds to $\dot{M}_1$ in our calculations. The evolution terminates with an evolved MS companion when $P_{\rm orb} \sim 18$ h and $M_2 \sim 0.2\,{\rm M}_\odot$ (see Figs 3b, c, and e). The observed properties of AMXPs with MS companions are shown in Fig. 3(f) together with the three models with $P_{\rm orb,i} = 1.2$, 2.1, and 2.8 d. The model tracks can simultaneously reproduce the observed properties (M_2, $\dot{M}_2$, and $P_{\rm orb}$; Figs 3b and f) of these AMXPs (with the exception of SAX J1748-2021).

The BD, UCXB, and MS tracks represent distinct evolutionary paths governed by AML through MB and GR. While the BD and UCXB tracks undergo early or delayed mass transfer leading to degenerate donors, the MS-tracks seem to correspond to the LMXB phase of UCXB-tracks ending with evolved MS companions. Each of these tracks produces a different mass transfer history, which we will use to investigate the rotational evolution of AMXPs in Section 3.

2.5 Effects of β and $\gamma_{\rm MB}$ on the binary evolution

The key `mesa` parameters that affect the binary evolution are β, $\gamma_{\rm MB}$, and $P_{\rm orb,i}$. To quantify the impact of these parameters, we performed a grid study in which we repeated the evolution of the illustrative Case 1 of the UCXB-track (see Section 2.4.2). We chose Case 1 because it is an illustrative binary evolution, undergoing two accretion phases at rates close to the Eddington limit during the LMXB and UCXB phases. Consequently, the NS experiences two distinct spin-up episodes, separated by a detachment phase. This allows an in-depth analysis of how the key `mesa` parameters affects both the binary evolution and the rotational evolution of the NS. We constituted the grid for four ($\gamma_{\rm MB}$, $P_{\rm orb,i}$) pairs: (2, 2.24 d), (3, 2.42 d), (4, 2.60 d), and (5, 2.79 d), and for $\beta = 0.2$, 0.4, 0.6, and 0.8. For each different

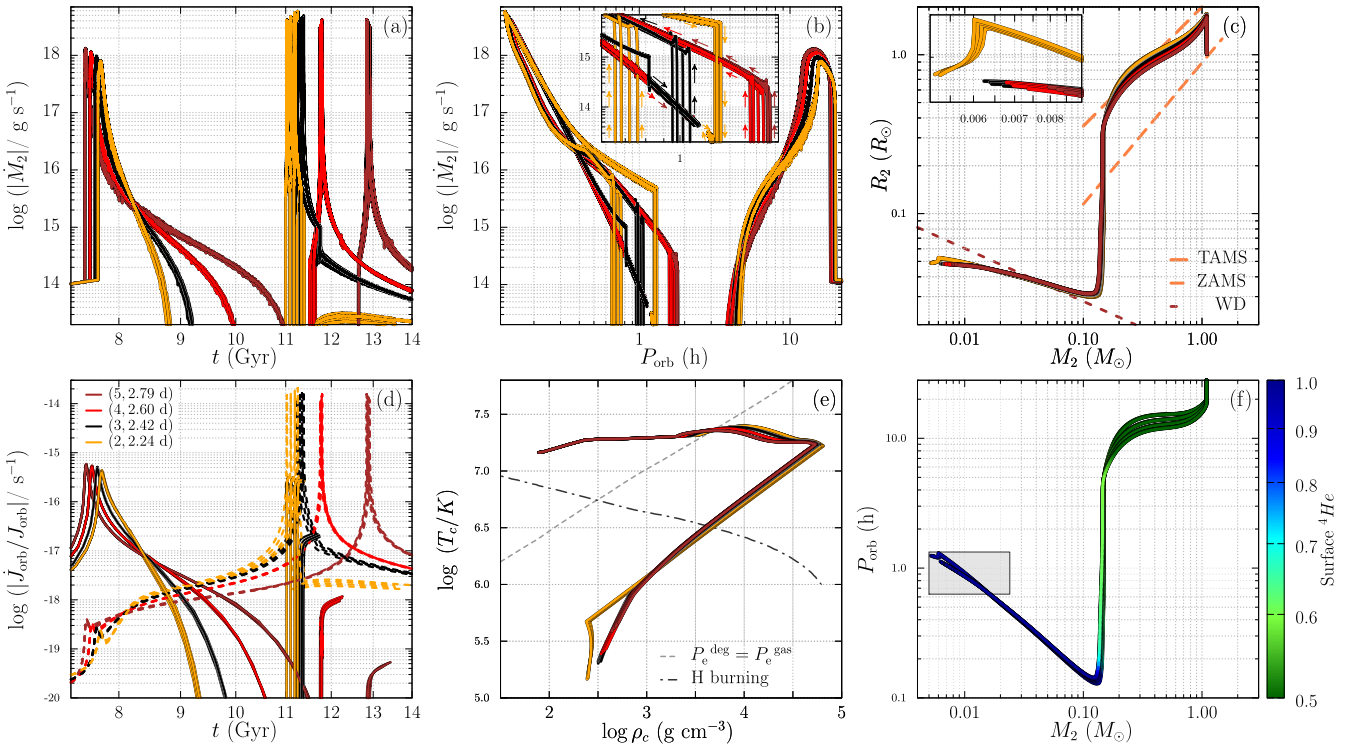

Figure 4. Same as Fig. 2. The effect of β and $\gamma_{\rm MB}$ is shown for the illustrative Case 1 of the UCXB-track through grid analysis. In panels (a)–(e), the values of ($\gamma_{\rm MB}$, $P_{\rm orb,i}$) pairs are (2, 2.24 d) for orange curves, (3, 2.42 d) for black curves, (4, 2.60 d) for red curves, and (5, 2.79 d) for brown curves.l for tfff In the zoom-in of (b) arrows indicate the directions followed by the curves. The zoom-in in (c) allows a better reading of final M_2 attained by the model curves.

$\gamma_{\rm MB}$ value, we adjusted $P_{\rm orb,i}$ by ~ 7 per cent in order to produce the same qualitative evolutionary sequence and enable a comparison of the resulting $\dot{M}_2$ histories. Fig. 4 shows the binary evolution of the 16 binary models, all of which satisfy the four criteria outlined in Section 2.4. In all cases, the donor ultimately acquires the characteristic properties of a He WD (Figs 4c, e, and f). The final donor masses obtained for different $\gamma_{\rm MB}$ values ($\sim 5.2 \times 10^{-3}$ M$_\odot$, $\sim 6.2 \times 10^{-3}$ M$_\odot$, $\sim 6.8 \times 10^{-3}$ M$_\odot$, and $\sim 7.7 \times 10^{-3}$ M$_\odot$) lie within ~ 15 per cent of the value obtained for Case 1 (see the zoom-in in Fig. 4c).

The most significant differences across the grid are seen in the $\dot{M}_2$ histories (Fig. 4a). While the detachment phase lasts ~ 2 Gyr in all 16 models, the duration of the LMXB phase increases systematically with increasing $\gamma_{\rm MB}$. This behaviour reflects the slower decay of MB torques for larger $\gamma_{\rm MB}$ values (Fig. 4d; see also S. Rappaport et al. 1983). Although MB torques are generally negligible compared to GR torques during the UCXB phase, they remain important for $\gamma_{\rm MB} = 2$ and 3. In particular, for $\gamma_{\rm MB} = 2$, the system operates close to a balance between MB and GR torques, leading $\dot{M}_2$ to decrease below 1×10^{11} g s^{-1}. The mass transfer resumes within $\simeq 2 \times 10^{-2}$ Gyr with $\dot{M}_2 \sim 10^{13}$ g s^{-1}. As a result, the corresponding evolutionary tracks do not terminate along the same branch as those obtained for $\gamma_{\rm MB} \geq 3$ (see the zoom-in in Fig. 4b). For a given ($\gamma_{\rm MB}$, $P_{\rm orb,i}$) pair, variations in β primarily affect $\dot{M}_2$, with lower (higher) β values yielding higher (lower) rates of mass transfer into the RL of the NS.

The results of a similar grid analysis for the BD and MS tracks show that for different $\gamma_{\rm MB}$ values, evolutionary curves with similar morphologies can be obtained by adjusting $P_{\rm orb,i}$ by a small percentage depending on $M_{2,\rm i}$. For instance, for a given $\gamma_{\rm MB}$ and $M_{2,\rm i}$ values of 1.1 M$_\odot$ and 1.3 M$_\odot$, we obtain similar model curves with ~ 7 per cent and ~ 13 per cent adjustments in $P_{\rm orb,i}$, respectively. For given $P_{\rm orb,i}$, different $\gamma_{\rm MB}$ values lead to qualitatively different evolutions. Models with $\gamma_{\rm MB} = 3$, 4, and 5 robustly remain on the same evolutionary track, differing mainly in the details of $\dot{M}_2$ history. In contrast, evolution with $\gamma_{\rm MB} = 2$ is very sensitive to $P_{\rm orb,i}$ such that small changes in $P_{\rm orb,i}$ could cause a transition to a different evolutionary track. This behaviour is reminiscent of the extreme fine-tuning problem identified by A. G. Istrate et al. (2014) for low $\gamma_{\rm MB}$.

Overall, this grid study demonstrates that the $\dot{M}_2$ histories are more sensitive to $\gamma_{\rm MB}$ than to β. The effect of these parameters is similar for the BD and MS tracks as well. We will also use the results of this grid study to investigate the effect of β and ($\gamma_{\rm MB}$, $P_{\rm orb,i}$) pairs on the NS rotational evolution in Section 3.7.

3 ROTATIONAL EVOLUTION OF AMXPS

3.1 The model

Here we briefly describe how the rotational phases and the inner disc properties of a source change with gradually increasing $\dot{M}_{\rm in}$ using an illustrative model source seen in Fig. 5 (for details, see U. Ertan 2021). In the model, there are three basic rotational phases: the SP, the WP, and the SU. At the lowest $\dot{M}_{\rm in}$ rates (lower than the rate corresponding to point B in Fig. 5), the system is in the SP phase with $r_{\rm in} > r_{\rm l} = 1.26\, r_{\rm co}$. Here, $r_{\rm co} = (GM_1/\Omega_\star^2)^{1/3}$ is the co-rotation radius, and $\Omega_\star$ is the angular spin frequency of the NS. In this phase, all the inflowing mass is thrown out of the system from the narrow inner boundary of the disc.

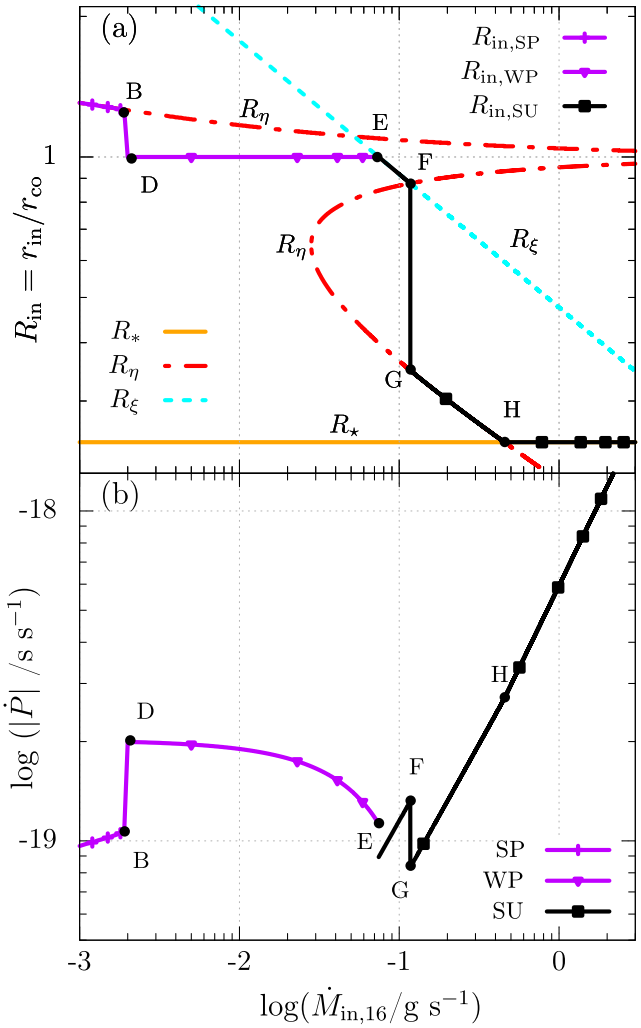

Figure 5. Variations of $R_{\rm in}$ (a) and $\dot{P}$ (b) with $\dot{M}_{\rm in}$ in the SP (solid curve with a plus sign), WP (solid curve with filled triangles), and SU phases (solid curve with filled squares). For this illustrative source, we take $r_\star = 1.2 \times 10^6$ cm, $\Delta r/r_{\rm in} = 0.2$, $\eta = 1.0$, $\xi = 0.5$, $B = \mu/r_\star^3 = 1 \times 10^8$ G, and $P = 10$ ms (see the text for details). In panel (a), the dot–dashed curves and dashed line represent $R_\eta(\dot{M}_{\rm in})$ and $R_\xi(\dot{M}_{\rm in})$, respectively, and the solid line shows $R_\star$. The points with letters in panel (b) indicate the same transitions shown in panel (a) with the SP phase beyond B, the WP phase between D and E, and the SU phase between points E and H.

The maximum inner disc radius, $r_{\rm in,max}$, at which the SP mechanism is sustainable is obtained from

$$R_{\rm in,max}^{25/8}\,|1 - R_{\rm in,max}^{-3/2}| \simeq 0.22\,\alpha_{\rm visc,-1}^{2/5}\,M_{1.4}^{-7/6}\,\dot{M}_{\rm in,16}^{-7/20}\,\mu_{26}\,P_{\rm ms}^{-13/12}, \quad (10)$$

where $R_{\rm in,max} = r_{\rm in,max}/r_{\rm co}$, $M_{1.4} = (M_1/1.4\,{\rm M}_\odot)$, $\dot{M}_{\rm in,16} = \dot{M}_{\rm in}/(10^{16}\ {\rm g\ s^{-1}})$, $\mu_{26} = \mu/(10^{26}\ {\rm G\ cm^3})$, μ is the magnetic dipole moment of the NS, $\alpha_{\rm visc,-1} = (\alpha_{\rm visc}/0.1)$ is the kinematic viscosity parameter (N. I. Shakura & R. A. Sunyaev 1973), and $P_{\rm ms}$ is the spin period in milliseconds (U. Ertan 2017). We also define the radii $R_\star = r_\star/r_{\rm co}$, where $r_\star$ is the NS radius, $R_\eta = \eta R_{\rm in,max} = \eta\ r_\eta/r_{\rm co}$ with $\eta \lesssim 1$, $R_\xi = \xi R_{\rm A} = \xi\ r_{\rm A}/r_{\rm co}$ with $\xi \sim 0.5 - 1$ (P. Ghosh & F. K. Lamb 1979). The variations of R_η (dot–dashed curves) obtained from the solution of equation (10) and R_ξ (dashed line) with $\dot{M}_{\rm in}$ are shown in Fig. 5(a) for an illustrative model source with $P = 5$ ms and $\mu_{26} = 10^{26}$ G cm^3.

For higher $\dot{M}_{\rm in}$, if $r_{\rm in}$ is instantaneously between $r_{\rm co}$ and r_1 the matter expelled from the inner disc returns back to the disc at larger radii causing a pile-up, which pushes the inner disc inwards down to $r_{\rm in} = r_{\rm co}$ (B - D). This switches on the accretion on to the NS taking the system into the WP phase. For a large range of $\dot{M}_{\rm in}$, the system can remain in the WP phase with $r_{\rm in} = r_{\rm co}$ while the spin-down torques dominate the spin-up torques produced by accretion (D - E) except when the star is close to the WP/SU transition. The inner disc can penetrate into $r_{\rm co}$ when the viscous stresses dominate the magnetic stresses around $r_{\rm co}$. This happens when $\dot{M}_{\rm in}$ exceeds the rate corresponding approximately to $r_{\rm in} = r_\xi = \xi\ r_{\rm A}$. The transition from the WP phase to the SU phase (torque reversal) also takes place at this stage. Beyond this critical rate, $r_{\rm in}$ tracks r_ξ for a narrow $\dot{M}_{\rm in}$ range (E - F) up to the point on the r_η solution, which is also calculated from equation 10. For $R_{\rm in} < 1$ ($r_{\rm in} < r_{\rm co}$) the solution of equation (10) is double valued with an unstable upper branch and a stable lower branch (see U. Ertan 2021, for details). For the $\dot{M}_{\rm in}$ rate at point F on the unstable branch, the inner disc propagates inwards, opening the field lines down to the radius corresponding to point G on the lower stable branch of r_η solution. With further increase in $\dot{M}_{\rm in}$, $r_{\rm in}$ decreases tracking the lower branch of r_η until $r_{\rm in} = r_\star$. Depending on the critical P and B values, in some cases the inner disc propagates directly on to the NS since $r_\star > r_\eta$ for the $\dot{M}_{\rm in}$ corresponding to this transition (for details, see U. Ertan 2021).

The total torque acting on the NS can be written as

$$\Gamma = \sqrt{GM_1 r_{\rm in}}\,\dot{M}_\star - \frac{\mu^2}{r_{\rm in}^3}\left(\frac{\Delta r}{r_{\rm in}}\right) - \frac{2}{3}\frac{\mu^2\Omega_\star^3}{c^3} \quad (11)$$

In this equation, the first term is the spin-up torque, $\Gamma_{\rm acc}$, which is associated with the mass accretion from the inner disc on to the NS (J. E. Pringle & M. J. Rees 1972). Here, $\dot{M}_\star$ is the accretion rate on to the star. The second term is a spin-down torque, $\Gamma_{\rm D}$, which arises from the interaction between the inner disc and the field lines within the boundary layer with radial width Δr. The third term is the magnetic dipole torque, $\Gamma_{\rm dip}$, also a spin-down torque. The $\dot{P}$ and $r_{\rm in}$ variations are seen in Fig. 5.

The total torques acting on the NS during each rotational phase are given as

$$\begin{cases} \Gamma = \Gamma_{\rm acc} + \Gamma_{\rm dip} & ({\rm SU};\ r_{\rm in} < r_{\rm co}) \\ \Gamma = \Gamma_{\rm acc} + \Gamma_{\rm D} + \Gamma_{\rm dip} & ({\rm WP};\ r_{\rm in} = r_{\rm co}) \\ \Gamma = \Gamma_{\rm D} + \Gamma_{\rm dip} & ({\rm SP};\ r_{\rm in} > r_1) \end{cases} \quad (12)$$

The model does not address the evaporation of the inner disc due to thermal instabilities at very low $\dot{M}_{\rm in}$ levels (J. Frank, A. King & D. Raine 2002).

3.2 Numerical calculations

Using `mesa`, we have studied the binary evolution for each of the evolutionary tracks and obtained their respective $\dot{M}_2$, $\dot{M}_1$, and M_1 evolution. For the model calculations, we take $r_\star = 12$ km, the moment of inertia $I \simeq 2\,M_1\,r_\star^2/5$, $\xi = 0.8$, $\eta = 0.8$, and $\Delta r/r_{\rm in} = 0.2$ for all the evolutionary tracks, which gave reasonable results in the earlier applications (A. A. Gençali et al. 2022; N. Niang et al. 2024) and discuss the effects of the model parameters on the rotational evolution of the NS in Section 3.6.

The magnetic field of recycled pulsars is estimated to decay during the early phases of the long-term evolution of LMXBs. The field decays rapidly via accretion-induced ohmic dissipation, on a time-scale much shorter than the time-scale of the spin-

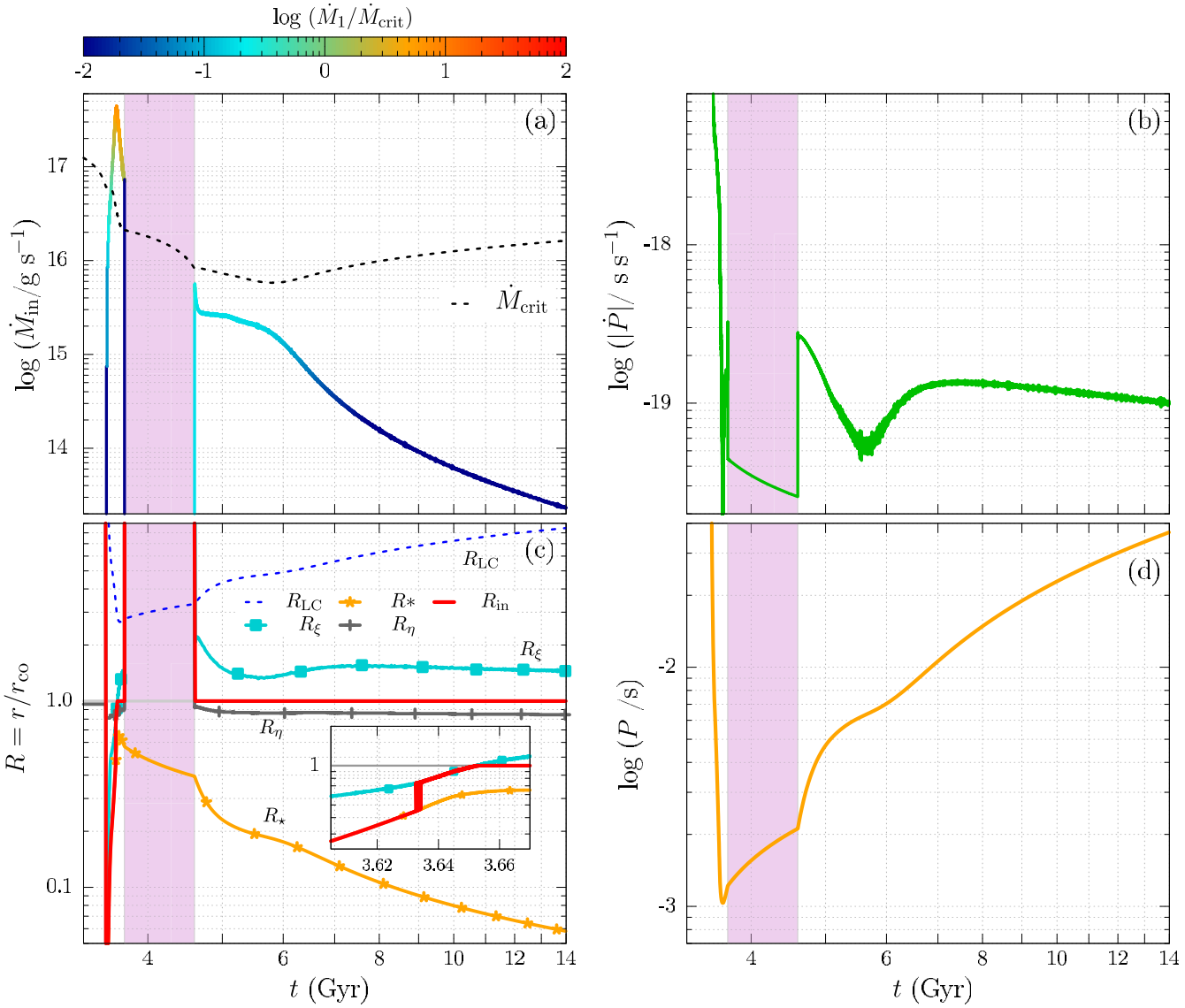

Figure 6. Evolution of the rotational properties of an NS evolving on the BD-track shown in Fig. 1. For all the curves, $r_\star = 1.2 \times 10^6$ cm, $\Delta r/r_{\rm in} = 0.2$, $\eta = 0.8$, $\xi = 0.8$, $B = \mu/R^3 = 2 \times 10^8$ G, $P_{\rm i} = 100$ s, and $P_{\rm orb,i} = 1.5$ d. (a) Evolution of $\dot{M}_{\rm in}$ with the colour bar indicating the ratio of $\dot{M}_1/\dot{M}_{\rm crit}$ and the dotted curve, $\dot{M}_{\rm crit}$. (b) Evolution of $\dot{P}$. (c) Evolution of $R_{\rm in}$ (solid curve), $R_{\rm LC}$ (dashed curve), R_ξ (solid curve with squares), R_η (solid curve with plus signs), and $R_\star$ (solid curve with stars). (d) Evolution of P. The shaded area indicate the RMSP phase.

up phase (U. Geppert & V. Urpin 1994; V. Urpin & U. Geppert 1995; S. Konar & D. Bhattacharya 1997; V. Urpin, U. Geppert & D. Konenkov 1998). The newly accreted material on the NS crust pushes the current-carrying layers towards deeper regions of higher density with higher conductivity. This slows down the field decay. The field ultimately freezes at a minimum strength $B_{\rm min}$ in the range of 10^7 G $\lesssim B_{\rm min} \lesssim 10^9$ G. The value of $B_{\rm min}$ is correlated with the long-term accretion rate (S. Konar & D. Bhattacharya 1997, 1999a, b; P. Halder et al. 2023). We take $B_{\rm min} = 2 \times 10^8$ G for our numerical computations and show the effect of different B values in Section 3.6.

Using the $\dot{M}_2$ value obtained from the `mesa` calculations, we calculate $\dot{M}_{\rm in} = \epsilon\, \dot{M}_2$. Each time interval dt and value of M_1 are calculated considering the current $\dot{M}_{\rm in}$ value obtained with `mesa` . Adjustable time-steps used by `mesa` could be too large (d$t > 10^2$ yr) to account for small P changes of the NS. We use much shorter dt values that can resolve the P variations of the NS, which also affect the $r_{\rm in}$ and torque calculations. Below we will describe the rotational evolution of NSs along the BD, UCXB, and MS tracks using illustrative model sources (Figs 6 – 8).

3.3 Rotational evolution of the NS on the BD-track

We obtain the model track seen in Fig. 6 with initial period, $P_{\rm i} = 100$ s and $P_{\rm orb,i} = 1.5$ d. The evolution of the NS starts in the SU phase at $t \simeq 3.5$ Gyr with $\dot{M}_{\rm in} \simeq 1 \times 10^{16}$ g s^{-1}. The inner disc reaches the NS surface within $\simeq 1.2 \times 10^{-3}$ Gyr with $\dot{M}_{\rm in} \simeq 3.5 \times 10^{17}$ g s^{-1} and $P \sim 0.1$ s. This situation persists for $\simeq 9.1 \times 10^{-2}$ Gyr effectively spinning the NS to $P \sim 2$ ms by $\Gamma_{\rm acc}$. The inner disc detaches from the NS surface when $P \simeq 1.9$ ms. A zoom-in of the detachment epoch is shown in Fig. 6(c). The system enters the WP phase at $t \simeq 3.6$ Gyr. $\dot{M}_{\rm in}$ remains close to its maximum value during the evolution, providing a strong $\Gamma_{\rm acc}$ spinning up the NS to its minimum $P \sim 1$ ms during the early

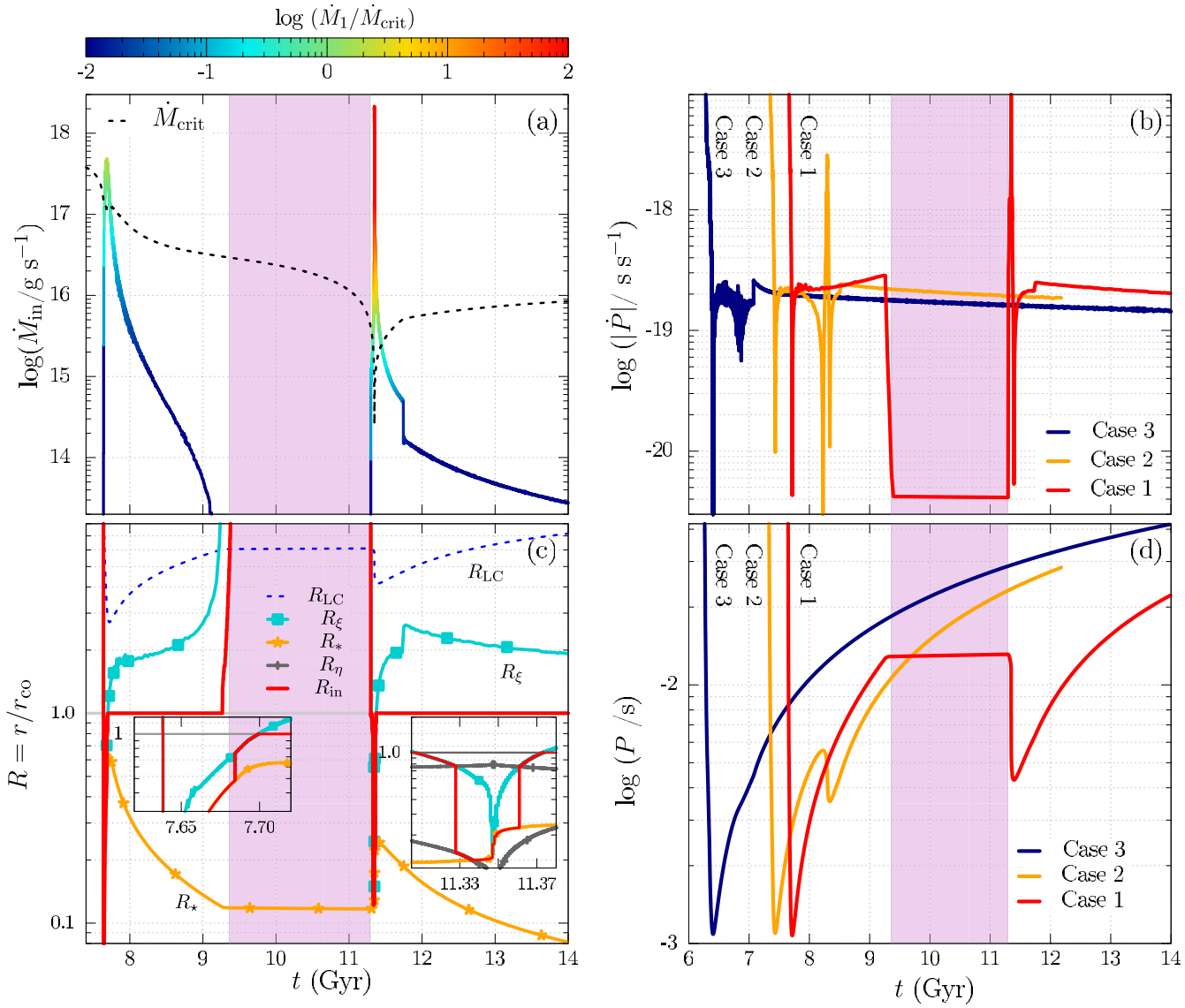

Figure 7. Same as Fig. 6 for an NS evolving on a UCXB-track with $P_{\rm orb,i} = 2.42$ d (Case 1), $P_{\rm orb,i} = 2.00$ d (Case 2), and $P_{\rm orb,i} = 1.90$ d (Case 3).

stages of the WP phase. Afterwards, $\dot{M}_{\rm in}$ decreases and the NS begins to spin-down at $t \simeq 3.67$ Gyr below $\dot{M}_{\rm in} \simeq 1 \times 10^{17}$ g s^{-1}.

The RLOF stops ($\dot{M}_{\rm in} = 0$) at $t \simeq 3.73$ Gyr and the system could be observable as an RMSP spinning down until $P \simeq 2.1$ ms (shaded area in Fig. 6). The RLOF resumes at $t = 4.6$ Gyr with $\dot{M}_{\rm in} \sim 3.0 \times 10^{15}$ g s^{-1}. The rotational evolution of the NS continues with the disc in the WP phase ($r_{\rm in} = r_{\rm co}$) slowing down mainly by $\Gamma_{\rm D}$ for the rest of its evolution. The system is a transient X-ray source during this late phase of evolution. $\dot{M}_{\rm in}$ remains close to $\sim 10^{15}$ g s^{-1} for another ~ 1 Gyr. We observe small fluctuations (torque reversals) in $\dot{P}$, which decrease while $\dot{M}_{\rm in}$ remains at the same level and P continues to increase from $P \sim 3$ ms to $P > 10$ ms during the long-term evolution (see Figs 6b and d). Overall, $\dot{P}$ decreases to a minimum value around 5×10^{-20} s s^{-1} and increases afterwards with decreasing $\dot{M}_{\rm in}$. It is highly likely that sources evolving along the BD-track are observed as AMXPs during this evolutionary phase. For this illustrative source, at $t \sim 4.6$ Gyr, the properties of the binary and its components are in good agreement with the observed properties of AMXPs with BD donors. For an NS with $B = 2 \times 10^8$ G, which is the median value of RMSPs, and $P_{\rm orb,i} = 1.5$ d, our results indicate that LMXBs with BD companions can form within 8 Gyr. Considering that donors in systems with smaller $P_{\rm orb,i}$ have shorter lifetimes, we estimate that some systems could form on a shorter time-scale.

3.4 Rotational evolution of the NS on the UCXB-track

We obtain the illustrative long-term evolution of the NS along the UCXB-track with $P_{\rm i} = 100$ s and $P_{\rm orb,i} = 2.42$ d. For this model source (Case 1), the evolution has two main phases: an LMXB phase and a UCXB phase (See Fig. 7). The RLOF begins in the SU phase at $t \simeq 7.63$ Gyr with $\dot{M}_{\rm in} \sim 2 \times 10^{16}$ g s^{-1}, and the inner disc moves inwards and reaches the NS surface with $\dot{M}_{\rm in} \sim 1 \times 10^{17}$ g s^{-1} within $\simeq 4.8 \times 10^{-3}$ Gyr. Starting from $t \simeq 7.64$ Gyr the NS rapidly spins up to $P \sim 1.7$ ms before the inner disc detaches from the NS surface at $t \simeq 7.68$ Gyr with $\dot{M}_{\rm in} \sim 4.5 \times 10^{17}$ g s^{-1}. The SU phase continues for $\sim 1 \times 10^{-2}$ Gyr (see the zoom-in Fig. 7c). The WP phase begins when $\dot{M}_{\rm in}$ de-

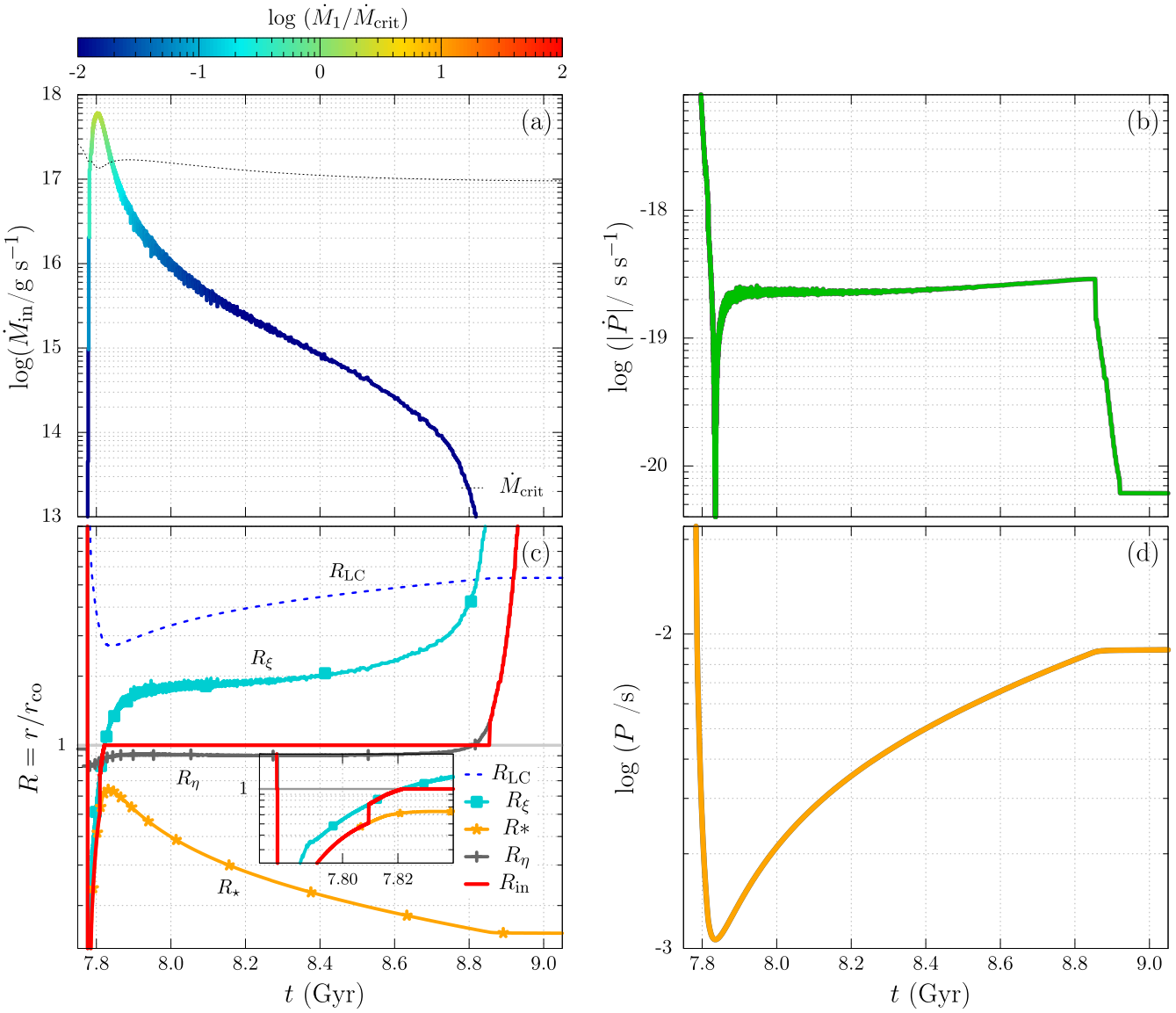

Figure 8. Same as Fig. 6 for an NS evolving on an MS-track with $P_{\rm orb,i} = 2.6$ d.

creases below $\sim 1 \times 10^{17}$ g s^{-1}. The NS spins up in the WP phase reaching its minimum $P \simeq 1.0$ ms around $t \simeq 7.72$ Gyr. As $\dot{M}_{\rm in}$ decreases below 5×10^{16} g s^{-1}, the system enters the transient regime and the NS starts to spin-down while the system is still in the WP phase, which persists for ~ 2 Gyr with $\dot{P} \sim 2 \times 10^{-19}$ s s^{-1}. The WP/SP transition takes place when $\dot{M}_{\rm in} \lesssim 1 \times 10^{11}$ g s^{-1} and $P \sim 12.4$ ms at $t \simeq 9.3$ Gyr. This marks the end of the LMXB phase, switching on the RMSP phase.

The UCXB phase starts with the onset of the second RLOF at $t \sim 11.3$ Gyr. The $\dot{M}_{\rm in}$ increases sharply from $\sim 1 \times 10^{11}$ to $\sim 1 \times 10^{15}$ g s^{-1} within ~ 1 Myr taking the system into the SU phase. After the WP/SU transition, the inner disc arrives at the NS surface within $\sim 3 \times 10^{-3}$ Gyr ($r_{\rm in} = r_\star$). Afterwards, the system accretes persistently while $\dot{M}_{\rm in}$ increases sharply to near the Eddington limit, with $\dot{M}_{\rm in} \sim 2 \times 10^{18}$ g s^{-1} on a time-scale of $\sim 1 \times 10^{-4}$ Gyr. During this epoch, the NS spins up rapidly from $P \sim 11.9$ ms to $P \sim 4.6$ ms. Subsequently, the inner disc detaches from the NS surface, and the system enters the WP phase when $\dot{M}_{\rm in} \lesssim 2 \times 10^{16}$ g s^{-1}. The minimum P (4.23 ms) for the UCXB phase is reached during this phase at $t \simeq 11.4$ Gyr. The NS spins down in the WP phase reaching gradually to the properties of $P \sim 22$ ms, $\dot{P} \sim 2 \times 10^{-19}$ s s^{-1}, and $\dot{M}_{\rm in} \sim 2.8 \times 10^{13}$ g s^{-1} at $t \simeq 14$ Gyr.

Figs 7(c) and (d) illustrate evolutions with different $P_{\rm orb,i}$ values corresponding to the three different cases discussed in Section 2.4.2. For Case 1 ($P_{\rm orb,i} = 2.42$ d), the NS is in the WP phase with $\dot{M}_{\rm in} \sim 5 \times 10^{14}$ g s^{-1}, $P \sim 6.0$ ms, and $\dot{P} \sim 2 \times 10^{-19}$ s s^{-1} between $t \simeq 11.5$ Gyr and $t \simeq 12.0$ Gyr. The observable properties of the system (binary, NS, and donor) at this epoch estimated by the model are very similar to observed properties of AMXPs with He WD donors. Similar observable properties are simultaneously observed between $t \simeq 8.3$ Gyr and $t \simeq 9.0$ Gyr for Case 2 ($P_{\rm orb,i} = 2.20$ d), and between $t \simeq 7.0$ Gyr and $t \simeq 7.8$ Gyr for Case 3 ($P_{\rm orb,i} = 1.90$ d) (see Figs 7b and d). Our results indicate that AMXPs that evolve on the UCXB-track can form within $\sim$ 8–12 Gyr.

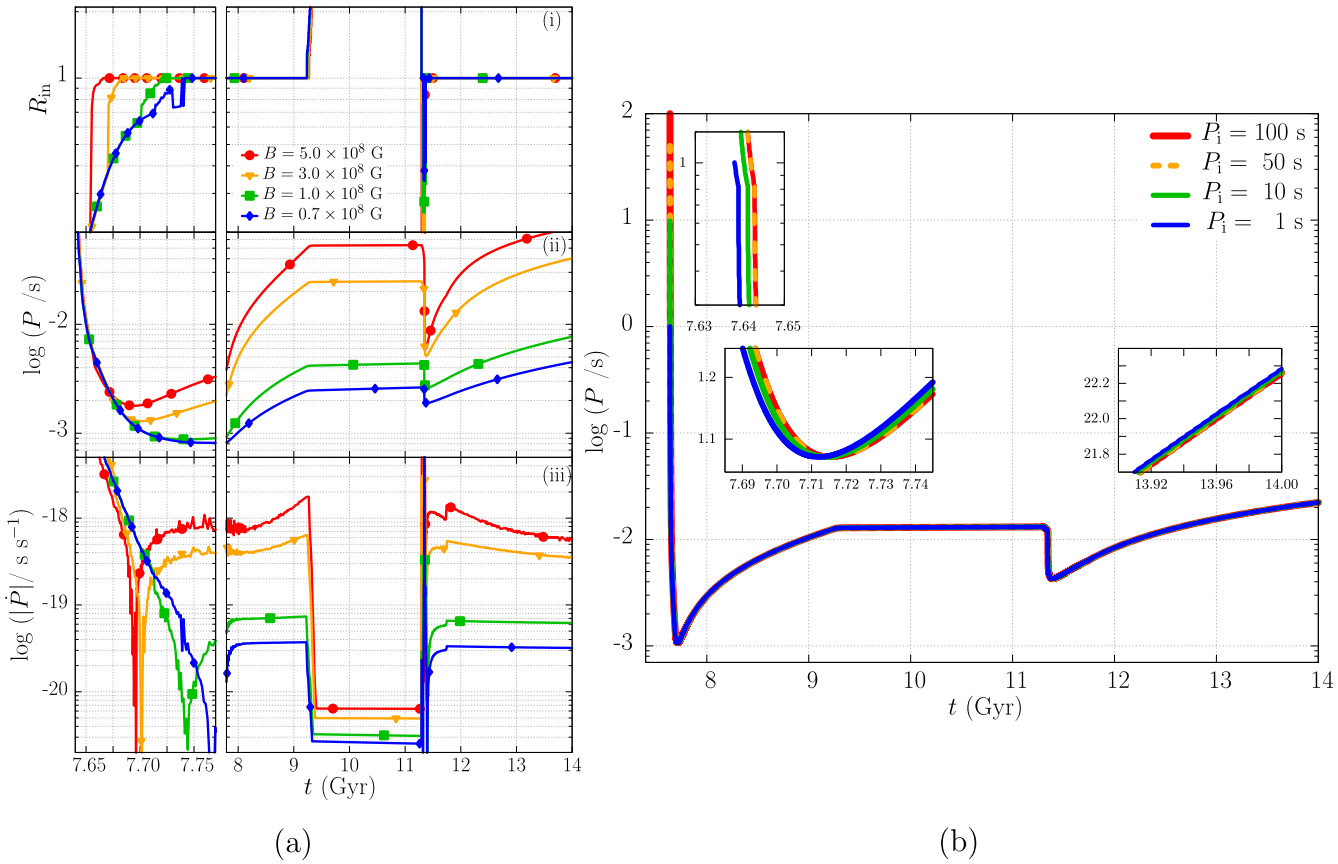

Figure 9. (a) Effect of different B values on the long-term evolution of $R_{\rm in}$, P, and $\dot{P}$ for $P_{\rm i} = 100$ s. (b) Effect of $P_{\rm i}$ on the long-term evolution of P for $B = 2 \times 10^8$ G. The model curves in (a) and (b) are obtained using the $\dot{M}_{\rm in}$ history of the binary model with $P_{\rm orb,i} = 2.42$ d (Case 1 in Section 3.4), $\xi = 0.8$, $\eta = 0.8$, and $\Delta r/r_{\rm in} = 0.2$.

3.5 Rotational evolution of the NS on the MS-track

The illustrative model curves seen in Fig. 8 are obtained with $P_{\rm i} = 100$ s and $P_{\rm orb,i} = 2.6$ d. The rotational evolution of this model source has the same morphology with the LMXB phase of the UCXB-track with $P_{\rm orb,i} = 2.42$ d (see Case 1, Section 3.4). RLOF (in the SU phase) begins at $t \simeq 7.77$ Gyr with $\dot{M}_{\rm in} \sim 2 \times 10^{16}$ g s^{-1}. The inner disc penetrates into $r_{\rm co}$ and reaches the surface of the NS within about 3×10^{-3} Gyr. While $r_{\rm in} = r_\star$ and $\dot{M}_{\rm in}$ increases to $\sim 5 \times 10^{17}$ g s^{-1}, the NS spins up to $P \sim 1.56$ ms until the inner disc detaches from the NS surface at $t \simeq 7.80$ Gyr. The spin-up continues until after the SU/WP transition (see the zoom-in Fig. 8c) and $P = 1.0$ ms and $\dot{M}_{\rm in} \sim 1 \times 10^{17}$ g s^{-1} at $t \simeq 7.83$ Gyr. For this illustrative source, the minimum P is reached during the WP phase. Afterwards, the NS spins down with further decrease in $\dot{M}_{\rm in}$, and the system enters the transient regime. During this epoch, $\Gamma_{\rm D}$ becomes the dominant torque with $\dot{P} \sim 2 \times 10^{-19}$ s s^{-1} (see Fig. 8d). The WP phase persists for ~ 1 Gyr across a large range of $\dot{M}_{\rm in}$. The NS enters the SP phase when $\dot{M}_{\rm in}$ falls below $\sim 10^{11}$ g s^{-1} at $t \simeq 8.8$ Gyr. Eventually, the RLOF ceases. The NS could be observed as an RMSP after the WP/SP transition. It is seen in Fig. 8 that the source has $P \sim 2.64$ ms, $\dot{P} \sim 2 \times 10^{-19}$ s s^{-1}, and $\dot{M}_{\rm in} \sim 4.5 \times 10^{15}$ g s^{-1} at $t \simeq 8.1$ Gyr while the system is evolving in the WP phase as a transient source. The state of the NS and the binary properties at this epoch are in good agreement with the observed properties of AMXPs with MS donors, which suggests that the model MS-track with $P_{\rm orb,i} = 2.6$ d is a reasonable evolutionary path for AMXPs.

3.6 Effect of $P_{\rm i}$ and B on the NS evolution

The model curves seen in Figs 6–9 are produced with the same parameters ($\xi = 0.8$, $\eta = 0.8$, and $\Delta r/r_{\rm in} = 0.2$). A detailed study for these parameters can be found in U. Ertan (2021). We use the illustrative model binary, Case 1 of the UCXB-track (see Section 3.4) to show the effect of B on $R_{\rm in}$, P, and $\dot{P}$ in Fig. 9(a), and the effect of $P_{\rm i}$ on the evolution in Fig. 9(b). It is seen in Fig. 9(a) that higher (lower) B values result in the earlier (later) SU/WP transitions occurring at higher (lower) $\dot{M}_{\rm in}$ levels. Additionally, NSs with stronger dipole fields evolve towards longer periods due to the B^2 dependence of the spin-down torques, $\Gamma_{\rm D}$ and $\Gamma_{\rm dip}$.

The long-term rotational evolution of model NSs shown in Figs 6–8 is obtained with $P_{\rm i} = 100$ s. To see the effect of $P_{\rm i}$ on our results, we repeated the calculations using $P_{\rm i} = 50$, 10 , and 1 s for each of the cases presented in Section 3.4. Fig. 9(b) shows zoomed-in views of the spin evolution at three evolutionary stages. The top-left panel corresponds to the onset of RLOF, marking the beginning of the SU phase ($t \simeq 7.64$ Gyr). The centre-left panel shows the phase when $\dot{M}_{\rm in}$ reaches its maximum ($t \simeq 7.71$ Gyr, $P \simeq 1.07$ ms). The centre-right panel corresponds to the end of the evolution ($t \simeq 14.00$ Gyr, $P \simeq 22.3$ ms). For the illustrative cases with $P_{\rm i} = 50$, 10 , and 1 s, the resulting spin evolutions remain within 1 per cent of the reference model with $P_{\rm i} = 100$ s at all evolutionary stages seen in Fig. 9(b). We find that, like P, $\dot{P}$ and $R_{\rm in}$ are also insensitive to $P_{\rm i}$.

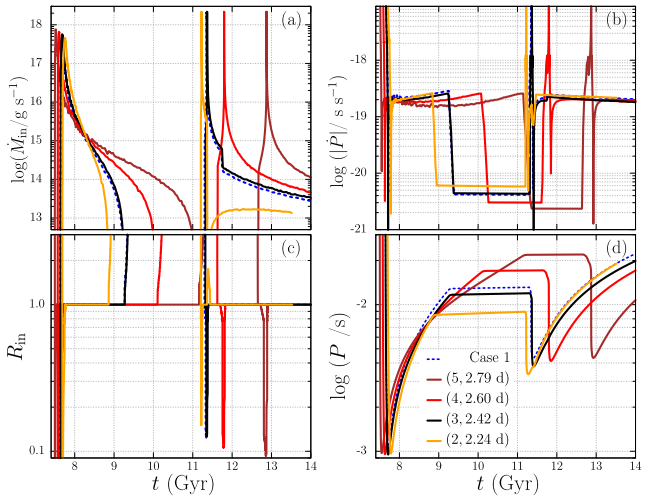

Figure 10. Same as Fig. 7 for ($\gamma_{\rm MB}$, $P_{\rm orb,i}$) pairs described in Section 2.5 (also given in the figure) and $\beta = 0.4$ together with the evolution of Case 1 shown by the blue dashed curves.

3.7 Effect of β and $\gamma_{\rm MB}$ on the NS evolution

Using the $\dot{M}_2$ histories from the grid analysis of Section 2.5, we examine the effects of β and $\gamma_{\rm MB}$ on the rotational evolution of the NS. We again use Case 1 for illustration of these effects, as it passes twice through the SU, WP, and SP phases with a detachment phase in between. Fig. 10 shows the long-term evolution of $\dot{M}_{\rm in}$, $\dot{P}$, $R_{\rm in}$, and P for $\beta = 0.4$ and the same four ($\gamma_{\rm MB}$, $P_{\rm orb,i}$) pairs used in Section 2.5. We also plot the evolution of Case 1 as our reference model for comparison. For each ($\gamma_{\rm MB}$, $P_{\rm orb,i}$) pair, the variations of $R_{\rm in}$ with $\dot{M}_{\rm in}$ (Figs 10a and c) in the SU, WP, and SP phases are consistent with those described in Section 3.4. Similarly, variations in $\dot{P}$ remain within a factor of 2 of the values obtained in Case 1 (Fig. 10b). $R_{\rm in}$ and $\dot{P}$ are moderately sensitive to β and $\gamma_{\rm MB}$ values, while the P evolution is highly sensitive to these parameters (Fig. 10d). During the first spin-up episode, P reaches a minimum of ~ 1 ms for all $\gamma_{\rm MB}$. The values obtained for $\beta = 0.2$, 0.6, and 0.8 remain within 3 per cent of the minimum values obtained for $\beta = 0.4$. During intermediate stages of the evolution (pre-detachment), we find that models with higher (lower) $\gamma_{\rm MB}$ values experience a stronger (weaker) spin-down as they spend more (less) time in the WP phase. Following the detachment phase, the system enters a second SU phase where the minimum period attained is $P \sim 4$ ms with β-dependent deviations rising to 12–22 per cent. This trend reverses at the end of the evolution, where longer final periods ($P \sim 20$ ms) are attained with lower $\gamma_{\rm MB}$, and the total dispersion across the β range reaches approximately 40 per cent. Overall, the varying effects of $\gamma_{\rm MB}$ and β on the rotational evolution are a direct consequence of how the variations of these parameters affect $\dot{M}_{\rm in}$ as we have shown in Section 2.5.

4 APPLICATIONS TO THE OBSERVED AMXPS

Here, we will present the applications of our analytical model together with the `mesa` code to the binary and NS properties of the three AMXPs selected from each of the three main binary tracks discussed in Section 3. The model parameters are given in figure captions (Figs 11–13). Using the observed properties of the sources that are available in the literature, we calculate the relative errors ($\theta(P) = |P - P_{\rm obs}|/P_{\rm obs}$) for each of these values calculated in our model. We look for a solution set of t, P, $\dot{P}$, $P_{\rm orb}$, M_2, and $\dot{M}_{\rm in}$ values for which the four criteria mentioned in Section 2.4 are met and $\theta(P)$ is equal to its minimum. Afterwards, we discuss the relative errors $\theta(\dot{P})$, $\theta(P_{\rm orb})$, $\theta(M_2)$, and $\theta(\dot{M}_{\rm in})$ in other observables. The evolution of the NS and the binary properties are given in Figs 11–13. In these figures, vertical grey strips show the time interval during which the model reproduces the observed NS and binary properties simultaneously. We select B values in the range of 10^7 to 10^9 G and take $\xi = 0.8$, $\eta = 0.8$, and $\Delta r/r_{\rm in} = 0.2$ to study the long-term evolution of HETE J1900.1-2455 (hereafter, J1900) for the BD-track, XTE J1751-305 (hereafter, J1751) for the UCXB-track, and Aql X-1 for the MS-track. Our results are summarized in Table 2.

HETE J1900.1-2455

The source J1900 was discovered during its X-ray outburst in June 2005 (R. Vanderspek et al. 2005), and coherent 2.65 ms X-ray pulsations were subsequently detected in July 2005 (P. Kaaret et al. 2006). The donor is a low-mass BD with $M_{2,\rm min} = 0.016\,{\rm M}_\odot$ and $P_{\rm orb} = 1.39$ h. J1900 exhibits sporadic X-ray pulsation behaviour, classifying it as an intermittent AMXP (T. Di Salvo & A. Sanna 2022). The distance to the source, $d = 4.7 \pm 0.6$ kpc, is estimated from the photospheric radius expansion (PRE) during an X-ray burst (D. K. Galloway et al. 2020). The source remained in outburst for a decade, until 2015 October (C. O. Heinke et al. 2025).

We obtain reasonable model curves that could represent the evolution of J1900, taking $M_{1,\rm i} = 1.4\,{\rm M}_\odot$, $M_{2,\rm i} = 1.1\,{\rm M}_\odot$, $\gamma_{\rm MB} = 3$, $\beta = 0.5$, and $P_{\rm orb,i} = 1.7$ d. For the NS evolving with the corresponding $\dot{M}_{\rm in}$ history, we take $P_{\rm i} = 100$ s and $B = 5 \times 10^7$ G. At $t \simeq 9.1$ Gyr, we obtain a solution for which $\theta(P) = 4.29 \times 10^{-6}$ (indicated by the grey strip in Fig. 11), $P_{\rm orb} \simeq 1.41$ h ($\theta(P_{\rm orb}) = 0.013$), and the donor is a hydrogen-poor BD with $M_2 \simeq 0.016\,{\rm M}_\odot$ ($\theta(M_2) = 0.081$). At this stage, the NS is in the WP phase with $M_1 = 1.93\,{\rm M}_\odot$, $\dot{M}_{\rm in} \simeq 8.6 \times 10^{13}$ g s^{-1}, and $\dot{P} \simeq 1.6 \times 10^{-20}$ s s^{-1}, which is also in agreement with the long-term secular $\dot{P}$ values observed in AMXPs during their quiescent states (A. Patruno & A. L. Watts 2021; T. Di Salvo & A. Sanna 2022).

XTE J1751-305

The source J1751 was discovered in 2002 with the detection of $P = 2.30$ ms X-ray pulsations during an X-ray outburst (C. B. Markwardt et al. 2002). The source showed outbursts again in 2005, 2007, and 2009, without any X-ray burst. The distance to the source is estimated to be ~ 8.5 kpc (C. O. Heinke et al. 2025). $P_{\rm orb} = 42.3$ min and the donor is a low-mass He WD with $M_{2,\rm min} = 0.013$–0.017 M$_\odot$ (C. J. Deloye & L. Bildsten 2003). We model the long-term rotational evolution of J1751 with $M_{1,\rm i} = 1.4\,{\rm M}_\odot$, $M_{2,\rm i} = 1.1\,{\rm M}_\odot$, $\gamma_{\rm MB} = 3$, $\beta = 0.5$, and $P_{\rm orb,i} = 2.41$ d. For the NS we take $P_{\rm i} = 100$ s and $B = 7 \times 10^7$ G. We find a reasonable solution at $t \simeq 11.4$ Gyr with $\theta(P) = 1.46 \times 10^{-4}$ (indicated by the grey strip in Fig. 12), when the NS has $P = 2.30$ ms, $P_{\rm orb} \simeq 48.8$ min ($\theta(P_{\rm orb}) = 0.15$), and the donor is a He WD with $M_2 \simeq 0.014\,{\rm M}_\odot$ ($\theta(M_2) = 0.184$). The NS is in the WP phase, with $M_1 = 1.93\,{\rm M}_\odot$, $\dot{M}_{\rm in} \simeq 1.73 \times 10^{14}$ g s^{-1} ($\theta(\dot{M}_{\rm in}) = 0.459$), and $\dot{P} \simeq 3.29 \times 10^{-20}$ s s^{-1} ($\theta(\dot{P}) = 0.136$). At this stage of the evolution, time-averaged $\dot{M}_{\rm in} = 3.21^{+1.64}_{-1.83} \times 10^{14}$ g s^{-1} estimated from about 10-yr long observations (C. O. Heinke et al. 2013). The measurements between the 2002 and 2009 outbursts give $\dot{P} = (2.9 \pm 0.6) \times 10^{-20}$ s s^{-1} (A. Riggio et al. 2011). It is seen in

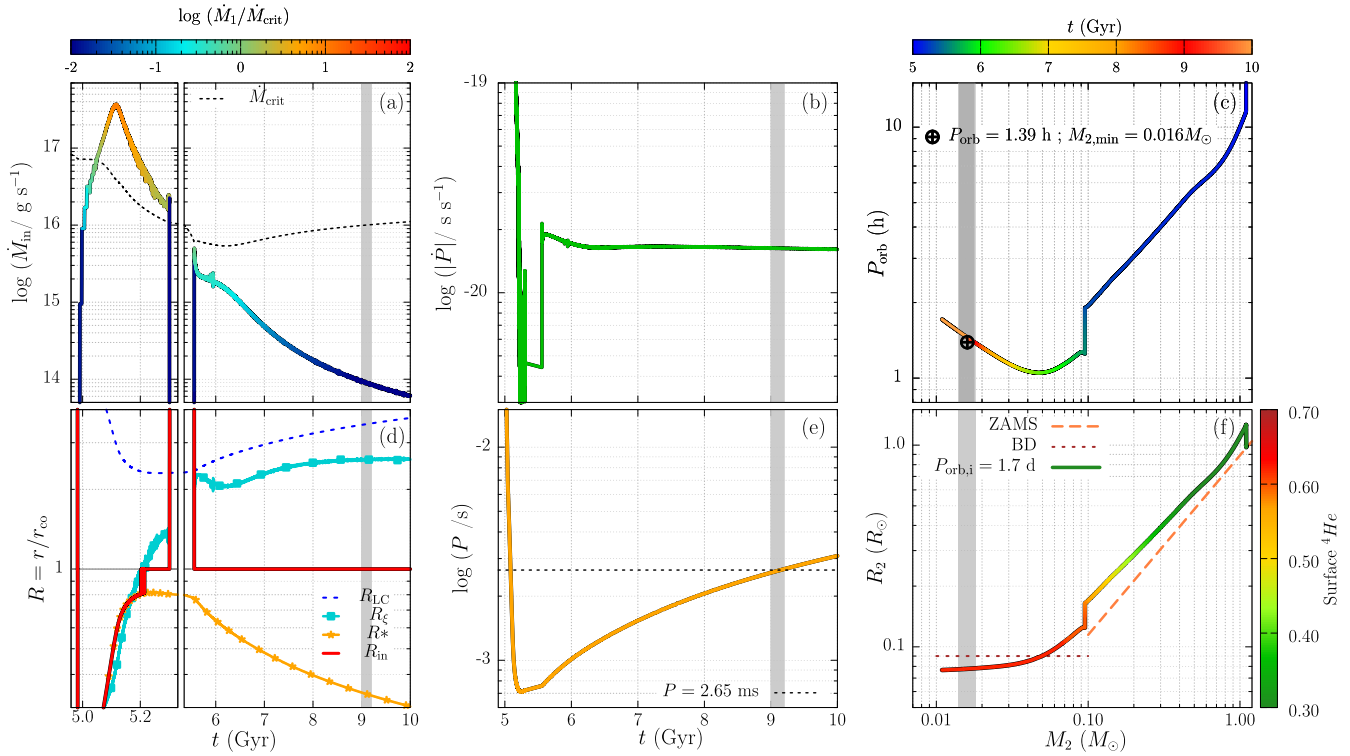

Figure 11. Evolution of the binary and rotational properties of J1900 obtained with $\Delta r/r_{\rm in} = 0.2$, $\eta = 0.8$, $\xi = 0.8$, $B = 5 \times 10^7$ G, $P_{\rm i} = 100$ s and $P_{\rm orb,i} = 1.7$ d. (a) Evolution of $\dot{M}_{\rm in}$ and $\dot{M}_{\rm crit}$ (dashed curve). The colour bar indicates $\dot{M}_1/\dot{M}_{\rm crit}$. (b) Evolution of $\dot{P}$. (c) Evolution of $P_{\rm orb}$ as a function of M_2. The colour bar shows the time in Gyr. (d) Evolution of $R_{\rm in}$ (solid curve), $R_{\rm LC}$ (dashed curve), R_ξ (solid curve with squares), and $R_\star$ (solid curve with stars). (e) Evolution of the NS's P. (f) Evolution of R_2 as a function of M_2. The colour bar indicates the evolution of the helium surface abundance for the companion. The vertical grey strips seen in each panel indicate the time at which the binary and the NS properties of J1900 are obtained simultaneously.

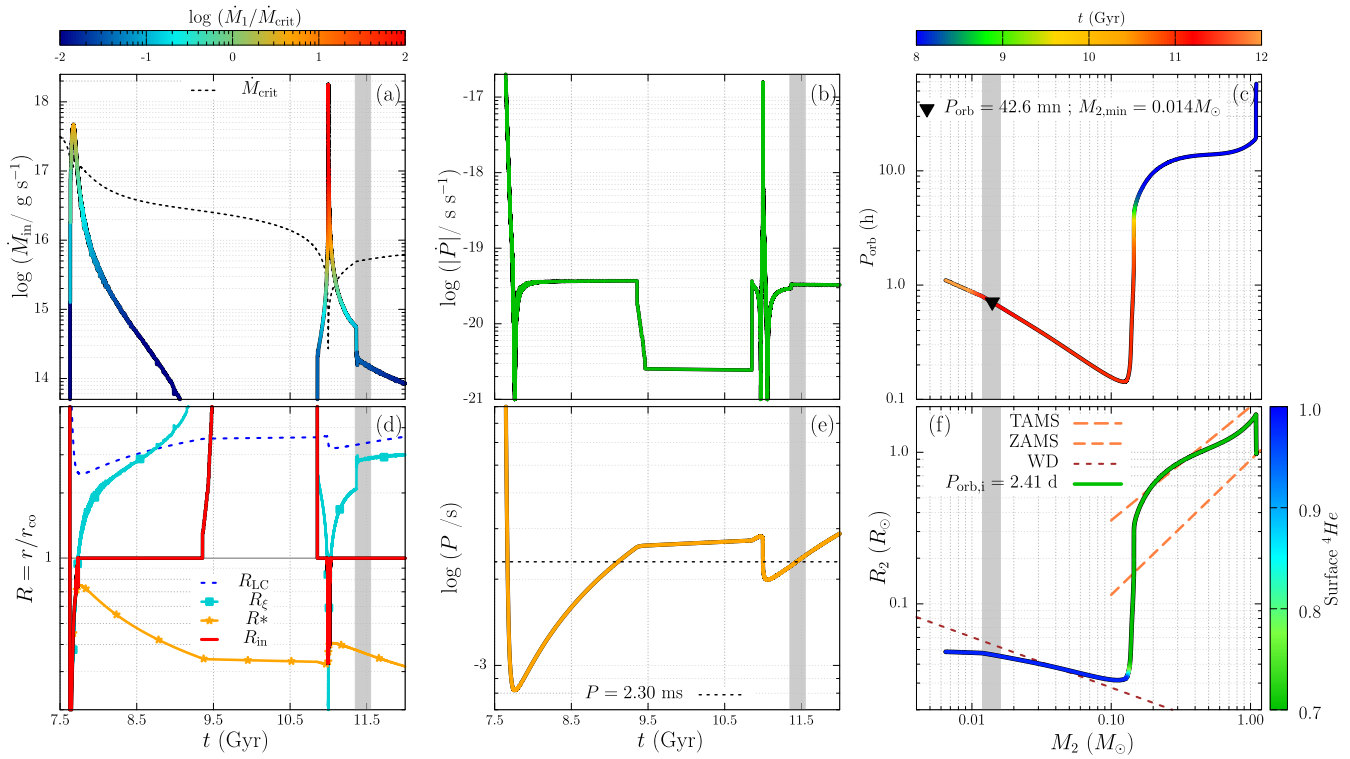

Figure 12. Evolution of the binary and rotational properties of J1751. Same as Fig. 11, except $P_{\rm orb,i} = 2.41$ d, and $B = 7 \times 10^7$ G. The vertical grey strips seen in each panel indicate the time at which the binary and the NS properties of J1751 are obtained simultaneously.

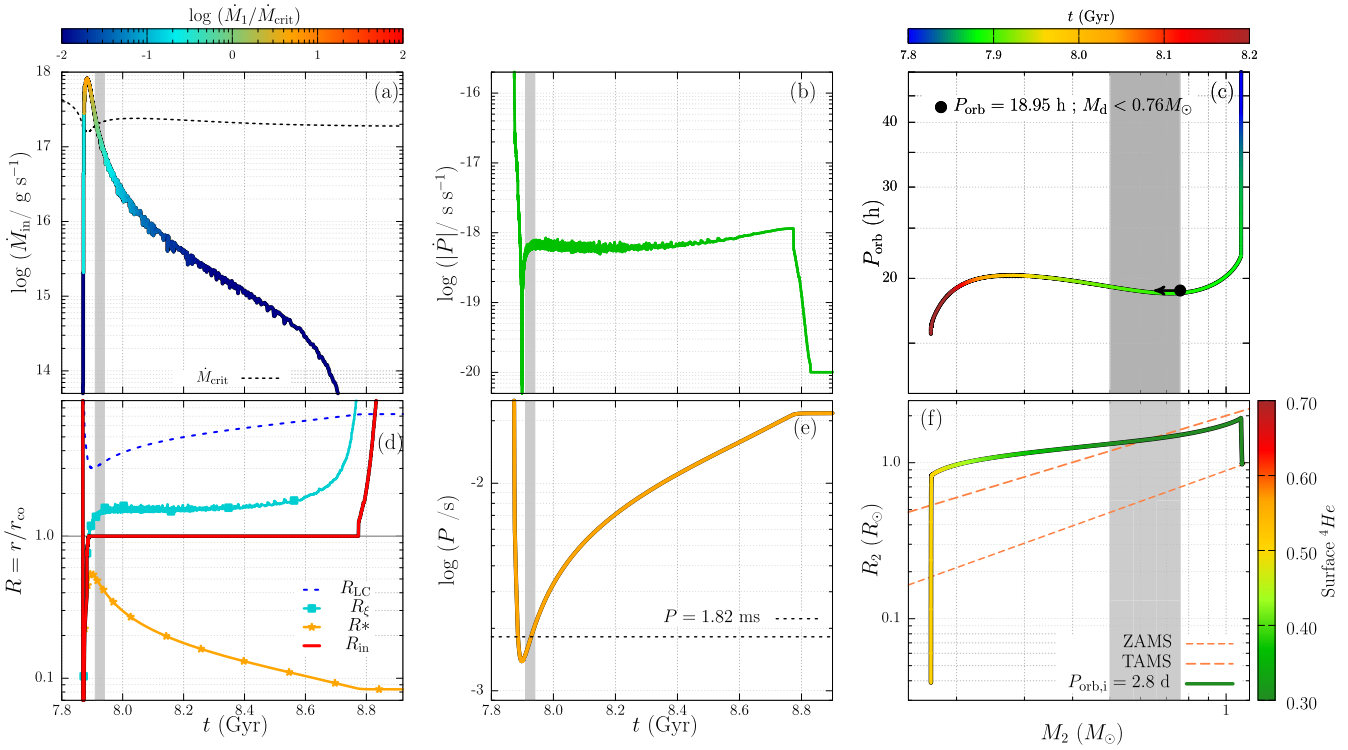

Figure 13. Evolution of the binary and rotational properties of Aql X-1. Same as Fig. 11, except $P_{\rm orb,i} = 2.8$ d, and $B = 4 \times 10^8$ G. The vertical grey strips seen in each panel indicate the time at which the binary and the NS properties of Aql X-1 are obtained simultaneously.

Table 2. Comparison of the observed properties (P, $\dot{P}$, $P_{\rm orb}$, M_2, and $\dot{M}_{\rm in}$) with the model sources for three AMXPs. The θ values show the relative errors described in Section 4.

Property		J1900	J1751	Aql X-1
P (ms)	Observed	2.6504377	2.2971710	1.817289
	Model	2.6504490	2.2968364	1.817543
	$\theta(P)$	4.29×10^{-6}	1.46×10^{-4}	1.39×10^{-4}
$P_{\rm orb}$ (h)	Observed	1.39	0.71	18.95
	Model	1.41	0.81	19.90
	$\theta(P_{\rm orb})$	0.013	0.15	0.05
M_2 ($M_\odot$)	Observed	0.016	0.014	0.56
	Model	0.017	0.011	0.38
	$\theta(M_2)$	0.081	0.184	0.32
$\dot{M}_{\rm in}$ (g s^{-1})	Observed	–	$3.21^{+1.64}_{-1.83} \times 10^{14}$	1.04×10^{17}
	Model	8.6×10^{13}	1.73×10^{14}	1.22×10^{17}
	$\theta(\dot{M}_{\rm in})$	–	0.459	0.08
$\dot{P}$ (s s^{-1})	Observed	–	2.9×10^{-20}	–
	Model	1.6×10^{-20}	3.2×10^{-20}	6.1×10^{-19}
	$\theta(\dot{P})$	–	0.136	–
$t_{\rm solution}$ (Gyr)		9.14	11.43	7.92

Fig. 12 that both measurements are in good agreement with the properties of the model at $t \simeq 11.4$ Gyr. In Fig. 12(e), the P curve estimated in the model is given by the solid curve and the dashed curve indicates the P of J1751. The two curves intersect four times during the rotational evolution of the source, but only the last intersection simultaneously matches the current NS and binary properties of J1751 in the WP phase; this is not the case for the first three intersections.

Aql X-1

Aql X-1 was discovered in 1991 with $P_{\rm orb} = 18.95$ h (C. Chevalier & S. A. Ilovaisky 1991) and a $K4 \pm 2$ MS donor star with $M_2 < 0.76\,M_\odot$ (D. M. Sánchez et al. 2017) during an X-ray outburst. Aql X-1 is observed in annual outbursts with occasional X-ray bursts. The distance is estimated to be ~ 4.5 kpc from the PRE (D. K. Galloway et al. 2008). Coherent $P = 1.82$ ms X-ray pulsations that lasted for ~ 150 s were recovered from archival data making the source an intermittent AMXP (P. Casella et al. 2008). The model curves seen in Fig. 13 are obtained with $M_{1,\rm i} = 1.4\,M_\odot$, $M_{2,\rm i} = 1.1\,M_\odot$, $\gamma_{\rm MB} = 3$, $\beta = 0.5$, and $P_{\rm orb,i} = 2.80$ d. Using the corresponding $\dot{M}_{\rm in}$ history, we obtain the NS evolution seen in Fig. 13 with $P_{\rm i} = 100$ s and $B = 4 \times 10^8$ G. For this illustrative evolution, the NS acquires $P = 1.82$ ms ($\theta(P) = 1.39 \times 10^{-4}$), $P_{\rm orb} = 19.9$ h ($\theta(P_{\rm orb}) = 0.05$) while the donor is an MS star with $M_2 \simeq 0.4\,M_\odot$ ($\theta(M_2) = 0.323$) at $t \simeq 7.9$ Gyr. All these binary and NS properties predicted by the model for $t \simeq 7.9$ Gyr are close to the values estimated from the observations. In the model, the MS value at $t \simeq 7.9$ Gyr is also close to the reported $M_2 \simeq 0.6\,M_\odot$ for an inclination sin $(i) = 1$ (T. Di Salvo & A. Sanna 2022). At this time of evolution, we find the NS in the WP phase as a transient source with $M_1 = 1.75\,M_\odot$, $\dot{M}_{\rm in} \simeq 1.2 \times 10^{17}$ g s^{-1} ($\theta(\dot{M}_{\rm in}) = 0.08$), and $\dot{P} \simeq 6.1 \times 10^{-19}$ s s^{-1}.

Table 2 compares the model results with the observed properties of the three sources. It is seen that the model yields reasonable results that are consistent with the binary and individual NS properties for the three AMXP sources representing the three main evolutionary tracks. The observed properties and long-term spin-down behaviour of these three sources can be consistently reproduced within the WP phase during their transient evolution. In an independent work, the same torque model was applied to five AMXPs with known secular $\dot{P}$ values to investigate

the torques acting on these systems throughout their outburst-quiescence cycles (F. Ertuğrul, A. A. Gençali, Ü. Ertan, N. Niang, in preparation). Their results are consistent with the observed properties of both the outburst and quiescent states, together with the resultant secular spin-down of these AMXPs. In future work, the $\dot{M}_{\rm in}$ histories obtained from `mesa` will be used to investigate the rotational evolution of these sources, considering their transient $L_{\rm X}$ behaviours.

5 SUMMARY AND DISCUSSION

Using reasonable `mesa` model parameters (β and $\gamma_{\rm MB}$) similar to those employed in earlier works (S. Gossage, V. Kalogera & M. Sun 2023; A. Kar et al. 2024), we obtained binary evolutions leading to the properties of the three basic AMXP groups classified by their companions (BD, He WD, and MS). Our results are consistent with the observed binary properties of AMXPs. Next, we used these $\dot{M}_{\rm in}$ histories obtained from the `mesa` models as inputs into our torque model to calculate the rotational evolution of NSs evolving along the BD, UCXB, and MS tracks. We have explained the typical evolutionary stages and properties of AMXPs evolving on these tracks, using illustrative sources (Figs 1–3). We also described the rotational evolutionary phases and the inner disc properties of the NSs accompanying the binary evolution (Figs 6–8). Next, we applied the model to three sources selected from the three groups of AMXPs. The binary properties ($P_{\rm orb}$ and M_2) and the individual source properties (P and $\dot{P}$) are produced simultaneously for each of these sources (Figs 11–13).

In our binary analysis, all simulated models are consistent with the observational constraints defining viable AMXP evolutionary tracks. These systems evolve into transient sources within a Hubble time and simultaneously reproduce the observed ranges of M_2, $P_{\rm orb}$, surface composition, and donor type for each of the three groups of AMXPs. To assess the effect of key `mesa` parameters, we simulated 16 binary models across a grid of β and ($\gamma_{\rm MB}$, $P_{\rm orb,i}$) pairs. Our results show that while β influences the efficiency of mass transfer, the overall evolutionary behaviour-especially the $\dot{M}_2$ histories-is more sensitive to $\gamma_{\rm MB}$. Nevertheless, we find that $P_{\rm orb,i}$ remains the most influential parameter in determining the evolutionary track, as variations in $P_{\rm orb,i}$ can lead to fundamentally different donor types and final system properties. Within this framework, our combined binary and NS evolution favours $\gamma_{\rm MB} = 3$–5, whereas models with $\gamma_{\rm MB} = 2$ often require $P_{\rm orb,i}$ tuning.

With reasonable values of the model parameters (ξ, η, and $\Delta r/r_{\rm in}$), we find that the rotational evolution of the NS is not sensitive to $P_{\rm i}$, while it is very sensitive to B. Extending the results of our grid analysis to the rotational evolution of the NS, we find that the impact of $\gamma_{\rm MB}$ and β on the evolution directly reflects their influence on $\dot{M}_{\rm in}$ via $\dot{M}_2$.

In this study, we employed the τ-boosted MB prescription of VIH19 to obtain the $\dot{M}_{\rm in}$ histories of AMXPs, whereas A. Kar et al. (2024) adopted the conventional MB prescription of S. Rappaport et al. (1983). To order of magnitude, the resulting $\dot{M}_{\rm in}$ histories in the two studies are comparable. The most notable differences arise in the predicted NS rotational evolution. We argue that these differences are primarily due to $r_{\rm in}$ and associated torque calculations. Using the torque model of S. Bhattacharyya & D. Chakrabarty (2017), A. Kar et al. (2024) could not reproduce the rotational properties of fast-spinning AMXPs ($P \lesssim 3$ ms). Their study, which extensively explores the ($M_{2,\rm i}$, $P_{\rm orb,i}$) parameter space for convergent LMXBs, successfully reproduces the binary properties of these systems, while it fails to account for their NS rotational properties. They suggested that the transient accretion during the late evolutionary stages may solve this problem. By adopting the torque model of U. Ertan (2021), we were able to reproduce both the binary evolution and the NS rotational properties of the three AMXP groups self-consistently, by varying only $P_{\rm orb,i}$ for reasonable B and other model parameters.

6 CONCLUSIONS

We have investigated the long-term binary and accompanying NS evolution in LMXBs, focusing on the formation of AMXPs along three distinct evolutionary tracks that depend on the donor type: BD-track (BD donor), UCXB-track (He WD donor), and MS-track (MS donor). For an evolutionary model track to be counted as a reasonable representation of the evolution into one of these LMXB families, the model should simultaneously reproduce the M_2, R_2, $P_{\rm orb}$ values, and the surface composition consistent with the observations. Using the $\dot{M}_{\rm in}$ evolution estimated from these binary evolutions, we have analysed the evolution of the NS on these tracks separately. Our results on the binary evolution obtained using the `mesa` code can be summarized as follows. (1) the τ-boosted MB model yields evolutionary curves that are consistent with observed $L_{\rm X}$ levels of LMXBs, in agreement with the earlier studies (K. X. Van et al. 2019; Z.-L. Deng et al. 2021). (2) Among the initial conditions, $P_{\rm orb,i}$ is the most influential factor affecting the binary evolution. (3) $\gamma_{\rm MB}$, which affects the duration of a mass transfer epoch plays a greater role than β, which affects the efficiency of the mass transfer. (4) With slight adjustments to $P_{\rm orb,i}$, evolutionary paths with same $\dot{M}_2$ morphology can be obtained for different $\gamma_{\rm MB}$ and β values. (5) Our results favour $\gamma_{\rm MB} \geq 3$ values since $\gamma_{\rm MB} = 2$ may require parameter tuning to obtain results consistent with observations. The results of our evolutionary tracks are in good agreement with the observed properties of AMXPs, except for three AMXPs with BD donors. We have estimated that the effect of irradiation of the companion by the NS, which was not taken into account in this work, could account for these sources as well. The irradiation effect on the evolution of these systems will be studied in an independent work. Using the $\dot{M}_{\rm in}$ obtained with `mesa` for the three evolutionary tracks of AMXPs, we have employed the analytical model developed by U. Ertan (2021) to calculate the $r_{\rm in}$ and the torques acting on the NS during the long-term evolution. Our results show that the model can account for the evolution of the NSs in these systems in accordance with their binary evolution. Our model naturally accounts for the fast-spinning AMXPs ($P \lesssim 3$ ms) with degenerate donors, which A. Kar et al. (2024) found challenging to reproduce. With reasonable parameters, the model reproduces the observed properties (P and $\dot{P}$) of HETE J1900.1-2455, XTE J1751-305, and Aql X-1 representing the three evolutionary tracks, simultaneously with the donor type, M_2, and $P_{\rm orb}$. Using the `mesa` code, a similar study is required to investigate the formation of millisecond pulsars above the $P_{\rm bif}$ of AMXPs. Such evolutionary tracks that lead to the formation of divergent systems namely, RMSPs with $P_{\rm orb} > 10$ d, are a large group within the binary pulsar population.

ACKNOWLEDGEMENTS

We thank the anonymous referee for very useful comments that have considerably improved our manuscript. NN thanks Yuki Kaneko for useful comments that have improved the manuscript.

We acknowledge research support from Sabancı University, and from TÜBİTAK (The Scientific and Technological Research Council of Turkey) through grant 123F083.

DATA AVAILABILITY

The `mesa` inlists used in this study can be shared upon request.

REFERENCES

Alpar M. A., Cheng A. F., Ruderman M. A., Shaham J., 1982, Nature, 300, 728
Archibald A. M. et al., 2009, Science, 324, 1411
Avakyan A., Neumann M., Zainab A., Doroshenko V., Wilms J., Santangelo A., 2023, A&A, 675, A199
Bahramian A., Degenaar N., 2022, Phys. Scr., 1984, 87
Bassa C. G. et al., 2014, MNRAS, 441, 1825
Bhattacharya D., van den Heuvel E. P., 1991, Phys. Rep., 203, 1
Bhattacharyya S., Chakrabarty D., 2017, ApJ, 835, 4
Bildsten L. et al., 1997, ApJS, 113, 367
Casella P., Altamirano D., Patruno A., Wijnands R., van der Klis M., 2008, ApJ, 674, L41
Chen W. C., 2017, MNRAS, 464, 4673
Chen H. L., Chen X., Tauris T. M., Han Z., 2013, ApJ, 775, 27
Chevalier C., Ilovaisky S. A., 1991, A&A, 251, L11
Deloye C. J., 2008, in Bassa C., Wang Z., Cumming A., Kaspi V. M., eds, AIP Conf. Proc. Vol. 983, 40 Years of Pulsars: Millisecond Pulsars, Magnetars and More. Am. Inst. Phys., New York, p. 501 10.1063/1.2900285
Deloye C. J., Bildsten L., 2003, ApJ, 598, 1217
Deng Z.-L., Li X.-D., Gao Z.-F., Shao Y., 2021, ApJ, 909, 174
Di Salvo T., Sanna A., 2022, in Bhattacharyya S., Papitto A., Bhattacharya D., eds, Astrophysics and Space Science Library Vol. 465, Millisecond Pulsars. Springer-Verlag, Berlin, p. 87
Dubus G., Lasota J. P., Hameury J. M., Charles P., 1999, MNRAS, 303, 139
Echeveste M., Novarino M. L., Benvenuto O. G., De Vito M. A., 2024, MNRAS, 530, 4277
Eggleton P. P., 1983, ApJ, 268, 368
Ertan U., 2017, MNRAS, 466, 175
Ertan U., 2018, MNRAS, 479, L12
Ertan U., 2021, MNRAS, 500, 2928
Faulkner J., 1971, ApJ, 170, L99
Frank J., King A., Raine D., 2002, Phys. Today, 39, 398
Fromang S., Stone J. M., 2009, A&A, 507, 19
Galloway D. K., Muno M. P., Hartman J. M., Psaltis D., Chakrabarty D., 2008, ApJS, 179, 360
Galloway D. K. et al., 2020, ApJS, 249, 32
Gençali A. A. et al., 2022, A&A, 658, A13
Geppert U., Urpin V., 1994, MNRAS, 271, 490
Ghosh P., Lamb F. K., 1979, ApJ, 232, 259
Gossage S., Kalogera V., Sun M., 2023, ApJ, 950, 27
Halder P., Goswami S., Halder P., Ghosh U., Konar S., 2023, Res. Notes AAS, 7, 213
He X., Meng X.-C., Chen H.-L., 2019, Res. Astron. Astrophys., 19, 110
Heinke C. O., Ivanova N., Engel M. C., Pavlovskii K., Sivakoff G. R., Cartwright T. F., Gladstone J. C., 2013, ApJ, 768, 184
Heinke C. O., Zheng J., Maccarone T. J., Degenaar N., Bahramian A., Sivakoff G. R., Toor S., 2025, ApJS, 279, 57
Istrate A. G., M Tauris T., Langer N., 2014, A&A, 571, A45
Jermyn A. S. et al., 2023, ApJS, 265, 15
Kaaret P., Morgan E. H., Vanderspek R., Tomsick J. A., 2006, ApJ, 638, 963
Kar A., Ojha P., Bhattacharyya S., 2024, MNRAS, 535, 344
Konar S., Bhattacharya D., 1997, MNRAS, 284, 311
Konar S., Bhattacharya D., 1999a, MNRAS, 303, 588
Konar S., Bhattacharya D., 1999b, MNRAS, 308, 795
Lan S.-Y., Meng X.-C., 2023, ApJ, 956, L24
Lasota J. P., 2001, New Astron. Rev., 45, 449
Lovelace R. V. E., Romanova M. M., Bisnovatyi-Kogan G. S., 1999, ApJ, 514, 368
Markwardt C. B., Swank J. H., Strohmayer T. E., in 't Zand J. J. M., Marshall F. E., 2002, ApJ, 575, L21
Misra D., Koljonen K. I., Linares M., 2025a, MNRAS, 541, L58
Misra D., Linares M., Ye C. S., 2025b, A&A, 693, A314
Niang N., Ertan U., Gençali A. A., Toyran O., Ulubay A., Devlen E., Alpar M. A., Gügercinoğlu E., 2024, MNRAS, 532, 2133
Papitto A., de Martino D., 2022, in Bhattacharyya S., Papitto A., Bhattacharya D., eds, Millisecond Pulsars. Springer International Publishing, Cham, p. 157
Papitto A. et al., 2013, Nature, 501, 517
Patruno A., Watts A. L., 2021, in Belloni Tomaso M., Méndez M. Z. C., eds, Timing Neutron Stars: Pulsations, Oscillations and Explosions. Springer, Berlin, Heidelberg, p. 143
Pavlovskii K., Ivanova N., 2016, MNRAS, 456, 263
Paxton B., Bildsten L., Dotter A., Herwig F., Lesaffre P., Timmes F., 2011, ApJS, 192, 3
Paxton B. et al., 2013, ApJS, 208, 4
Paxton B. et al., 2015, ApJS, 220, 15
Paxton B. et al., 2018, ApJS, 234, 34
Paxton B. et al., 2019, ApJS, 243, 10
Podsiadlowski P., Rappaport S., Pfahl E. D., 2002, ApJ, 565, 1107
Pringle J. E., Rees M. J., 1972, A&A, 21, 1
Pylyser E. H. P., Savonije G. J., 1988, A&A, 191, 57
Pylyser E. H. P., Savonije G. J., 1989, A&A, 208, 52
Radhakrishnan V., Srinivasan G., 1982, Curr. Sci., 51, 1096
Rappaport S., Verbunt F., Joss P. C., Rappaport S., Verbunt F., Joss P. C., 1983, ApJ, 275, 713
Reimers D., 1975, MSRSL, 8, 369
Riggio A., Burderi L., Salvo T. D., Papitto A., D'Aì A., Iaria R., Menna M. T., 2011, A&A, 531, A140
Sánchez D. M., Muñoz-Darias T., Casares J., Jiménez-Ibarra F., 2017, MNRAS, 464, L41
Sanna A. et al., 2022, MNRAS, 516, L76
Sengar R., Tauris T. M., Langer N., Istrate A. G., 2017, MNRAS, 470, 6
Shakura N. I., Sunyaev R. A., 1973, A&A, 24, 337
Skumanich A., 1972, ApJ, 171, 565
Srinivasan G., 2010, New Astron. Rev., 54, 93
Srinivasan G., Bhattacharya D., Muslimov A. G., Tsygan A. J., 1990, Curr. Sci., 59, 31
Tauris T. M., 2012, Science, 335, 561
Tauris T. M., 2018, Phys. Rev. Lett., 121, 131105
Tauris T. M., van den Heuvel E. P. J., 2023, Physics of Binary Star Evolution. From Stars to X-ray Binaries and Gravitational Wave Sources. Princeton Univ. Press, Princeton
Urpin V., Geppert U., 1995, MNRAS, 275, 1117
Urpin V., Geppert U., Konenkov D., 1998, A&A, 331, 244
Ustyugova G. V., Koldoba A. V., Romanova M. M., Lovelace R. V. E., 2006, ApJ, 646, 304
Uzdensky D. A., 2004, Astrophys. Space Sci., 292, 573
Van K. X., Ivanova N., 2019, ApJ, 886, L31
Van K. X., Ivanova N., 2021, ApJ, 922, 174
Van K. X., Ivanova N., Heinke C. O., 2019, MNRAS, 483, 5595
Vanderspek R. et al., 2005, Astron. Telegram, 516, 1
Wijnands R., Van Der Klis M., 1998, Nature, 394, 344
Yang H.-R., Li X.-D., 2024, ApJ, 974, 298
Zdziarski A. A., Ziółkowski J., Bozzo E., Pjanka P., 2016, A&A, 595, A52

This paper has been typeset from a TEX/LATEX file prepared by the author.